Bromine speciation and partitioning in slab-derived aqueous fluids and silicate melts and implications for halogen recycling in subduction zones

Marion Louvel[1,2], Carmen Sanchez-Valle[2], Wim J. Malfait[3], Gleb S. Pokrovski[4], Camelia N. Borca[5] and Daniel Grolimund[5]

[1]School of Earth Sciences, Bristol University, UK- BS81RJ, Bristol, United-Kingdom

[2]Institute for Mineralogy, WW-Universität Münster, D-48149, Münster, Germany

[3]Swiss Federal Laboratories for Materials Science and Technology EMPA, CH-8600, Dubendorf, Switzerland

[4]Groupe Métallogénie Expérimentale, Géosciences Environnement Toulouse (GET - UMR 5563), OMP-CNRS-IRD-University of Toulouse III Paul Sabatier, 31400 Toulouse, France

[5]Swiss Light Source, Paul Scherrer Institute, CH-5232, Villigen, Switzerland

Correspondence to: Marion Louvel (louvel@uni-muenster.de)

Abstract. Understanding the behavior of halogens (Cl, Br, and I) in subduction zones is critical to constrain the recycling of trace elements and metals, and to quantify the halogen fluxes to the atmosphere *via* volcanic degassing. Here, the partitioning of bromine between coexisting aqueous fluids and hydrous granitic melts and its speciation in slab-derived fluids have been investigated *in situ* up to 840 °C and 2.2 GPa by X-ray fluorescence (SXRF) and x-ray absorption spectroscopy (XAS) in diamond-anvil cells. The partition coefficients $D^{f/m}_{Br}$ range from **~2 to ~15, with an average value of 6.7 ±3.6 (SD) over the whole pressure-temperature *(P-T)* range, indicating a moderate Br enrichment in aqueous fluids, in agreement with previous work.** EXAFS analysis further evidences a gradual evolution of Br speciation from hydrated Br ions $[Br(H_2O)_6]^-$ in slab dehydration fluids to more complex structures invoving both Na ions and water molecules, $[BrNa_x(H_2O)_y]$, in hydrous silicate melts and supercritical fluids released at greater depth (> 200 km). In denser fluids (ρ > 1.5 g.cm^{-3}), containing 60 wt% dissolved alkali-silicates and in hydrous $Na_2Si_2O_5$ melts (10 wt% H_2O), Br is found to be in a "salt-like" structure involving 6 nearest Na ions and several next-nearest O neighbors that are either from water molecules and/or the silicate network. Bromine (and likely chlorine and iodine) complexing with alkalis is thus an efficient mechanism for the mobilization and transport of halogens by hydrous silicate melts and supercritical fluids. Our results suggest that both shallow dehydration fluids and deeper silicate-bearing fluids efficiently remove halogen from the slab in the sub-arc region, thus favoring an efficient recycling of halogens in subduction zones.

Keywords: Halogen cycle , speciation and partitioning, slab fluids subduction zones, diamond anvil cell.

1 Introduction

The fluxes of volatile elements (water, carbon, sulfur, and halogens) in subduction zones play a critical role in the Earth's chemical evolution**; however, the mecanisms and extent of their transfer from slab components to the mantle wedge, the volcanic arc and, ultimately, the atmosphere remain poorly understood.** Although halogens (F, Cl, Br and I) are rather minor volatiles compared to H_2O and CO_2, their effect on the physical and chemical properties of slab-derived fluids and arc magmas (*e.g.* phase equilibria, viscosity, density), as well as their ability to bind to **trace elements and base metals (e.g., Au, Cu, Zn, Pb)** makes them key players in the chemical transfer in subduction zones **and formation of ore deposits** (Zellmer et al., 2015; Barnes et al., 2018). Furthermore, their emission to the troposphere and stratosphere at volcanic arc centres may have **a** significant environmental impact, including ozone depletion by Br (Bobrowski et al., 2003; von Glasow et al., 2009; Kutterolf et al., 2013). Constraining the halogen cycle in subduction zones is thus crucial for assessing their impact on the global atmospheric chemistry and climate.

In the last decade, new developments in quantification techniques on pore fluids, fluid inclusions and rocks as well as in detection methods for halogens species in volcanic gases enabled better estimates of halogen fluxes in subduction zones (Wallace, 2005; Pyle and Mather 2009; John et al., 2011; Kendrick et al., 2013; Kendrick et al., 2015; Chavrit et al., 2016; Barnes et al., 2018). For example, comparisons of the input from the subducted sediments, altered oceanic crust and serpentinized oceanic lithosphere to the output along volcanic arcs point to a significant imbalance between fluorine input and output, suggesting a significant amount of F may be recycled into the mantle (Roberge et al., 2015; Grutzner et al., 2017). On the contrary, Cl, Br and I appear to be efficiently recycled up to the surface, either through shallow loss of fluids to the fore-arc region (Br and especially I) or deeper release upon slab dehydration

(especially Cl and Br, and to a lesser extent I) (Kendrick et al., 2018). Yet, the poor understanding of the transfer mechanisms and recycling paths of halogens limits the development of integrative numerical models constraining the role of fluids and halogens in the global cycling of elements in subduction zones (Ikemoto and Iwamori, 2014; Kimura et al., 2016). There is for instance virtually no constraint on the amounts of residual halogens that may be stored in the dehydrated slab or lost through hidden hydrothermal activity and passive degassing in the continental crust. Similarly, current knowledge of halogens solubility and speciation in fluids and melts is mostly limited to pressures below 0.3 GPa (equivalent to ~10 km depth), which are relevant to volcanic degassing and ore deposit formation in the shallow crust, but not to slab dehydration or melting beneath arcs at far greater depth (Webster, 1990; Métrich and Rutherford, 1992; Webster, 1992; Bureau et al., 2000; Signorelli and Carroll, 2002; Bureau and Métrich, 2003; Carroll, 2005; Evans et al., 2009; Cadoux et al., 2018). Only recently, Bureau et al. (2010, 2016) reported fluid-melt partition coefficients for Br and I in the haplogranite-H_2O system up to 1.7 GPa while Cochain et al. (2015) investigated the speciation of Br in aqueous fluids or haplogranitic melts up to 7.6 GPa. Nevertheless, the effect of fluid chemistry on the speciation and partitioning of halogens at high pressures and temperatures (*P*-*T*) is unknown in subduction zones. To fill this gap, we combine Synchrotron X-ray Fluorescence (SXRF) and X-ray Absorption Spectroscopy (XAS) measurements in a hydrothermal diamond-anvil cell (HDAC) to investigate Br fluid-melt partitioning and speciation in aqueous fluids and hydrous silicate melts that mimic the mobile phases released by the slab at sub-arc depths (Manning, 2004; Frezzotti and Ferrando, 2015). Bromine is employed here as an analog of chlorine amenable to SXRF and XAS studies through the diamond window of the HDAC due to its higher absorption edge energy (13.47 keV for bromine K-edge compared to 2.82 keV for chlorine K-

edge; Sanchez-Valle, 2013). Furthermore, among the halogens, bromine displays the closest behavior to chlorine in terms of solubility, partitioning and speciation in silicate melts, at least at shallow depth (Bureau et al., 2000, Bureau and Metrich, 2003; Wasik et al., 2005; Bureau et al., 2010; Cadoux et al., 2018). Bromine therefore represents the best analog of Cl for *in-situ* studies at high pressure (*P*) and high temperature (*T*) conditions. Our experimental results reveal systematic changes in Br speciation that reflect changes in fluid composition with depth; these new findings enable better constraints on the mechanisms controlling the transfer of halogens from the slab to arc magmas.

2 Methods

2.1 Starting materials

The speciation and fluid-melt partitioning experiments were conducted using 3 wt% NaBr aqueous solutions and synthetic sodium disilicate (NS2: $Na_2Si_2O_5$) or haplogranite (Hpg) glasses doped with 1 to 4 wt% Br as starting materials (Table 1). The 3 wt% NaBr aqueous solution was freshly prepared from distilled de-ionized water and analytical grade NaBr powder, sealed in tight containers and refrigerated until the experiments. The NS2 and Hpg glasses were synthesized in a piston-cylinder apparatus at 1200 °C and 0.5 GPa and 1.5 GPa, respectively, following the method described in Louvel et al. (2013). Briefly, reagent grade SiO_2 and Na_2SiO_3 were employed for the NS2 glasses whereas reagent grade SiO_2, Al_2O_3 and alkali-carbonates, K_2CO_3 and Na_2CO_3, were mixed for the haplogranite glass synthesis. Bromine was added as NaBr together with 3.3 wt% H_2O for the synthesis of the haplogranite glass to ensure complete melting and homogeneization of the sample at run conditions.

Major element (Si, Al, K and Na) contents and distribution in the glass were measured by by electron microprobe analyzer (EPMA) using a JEOL JXA-8200 microprobe **with an**

accelerating voltage of 15 keV, a 10 nA beam current and a defocused beam of 30 µm to avoid element migration during the analysis (Table 1). The probe was calibrated using wollastonite/quartz (Si), corundum (Al), aegirine (Na), K-feldspar (K), and counting time set to 40 s. The homogeneity of the glasses was confirmed by elemental profiles collected across the sample and by the absence of microscopic mineral phases. EPMA measurements of Br are hindered by i) the high ionization potential for the K-lines of Br resulting in low count rates; ii) the peak overlap between the L-lines of Br and the K-lines of Al; and iii) the lack of matrix-matched standards. To overcome these limitations, the concentration of Br in Hpg-Br2 glass sample was **first** determined by Rutherford Backscattering Spectroscopy (RBS) **at the Department of Physics of ETH Zurich.** This technique provides absolute elemental concentrations and is particularly appropriated for quantifying heavy elements in a light matrix as it is the case of Br in silicate glasses (Feldman and Mayer, 1986; Chu and Liu, 1996). **A 3.5 mm diameter disk of Hpg-Br2 glass, mounted in epoxy and carbon-coated, was exposed to a 2 MeV ^{4}He ion beam. The concentration of Br in the sample was determined from the energy of the backscattered alpha particles $^{4}He^{2+}$, yielding** a Br concentration of 0.96 ± 0.04 wt%, which is identical to the nominal Br concentration within analytical uncertainties (Table 1). This well-characterized sample was then used as a standard for Br analysis by EPMA and LA-ICPMS in the other glass samples **(NS2 and Hpg-Br3 – Table 1). EPMA characterization of Br was conducted with an accelerating voltage of 25 keV, a 90 nA beam current and a defocused beam of 30 µm. The signal from Br (and Na) was carefully monitored during the measurements and found to be stable for these conditions. Br concentrations in NS2-Br1 were also cross-checked by LA-ICPMS analyses that were conducted using a 193-nm ArF excimer laser coupled with an ELAN 6100 DRC ICP quadrupole mass spectrometer**

(Heinrich et al., 2003) and a beam diameter of 40 µm. All analyses were bracketed by measuring an external standard (NIST 610) to allow for linear drift correction, and the average SiO_2 and Br content determined by EPMA analysis for the Hpg-Br2 glass was used as the internal standard.

2.2 Hydrothermal diamond anvil cell experiments

All experiments were conducted in Bassett-type hydrothermal diamond-anvil cells (HDAC, Bassett et al., 1993) widely used for *in-situ* SXRF and XAS measurements on aqueous fluids and silicate melts up to 1000 °C and about 3 GPa (e.g., Borchert et al., 2009; Louvel et al., 2013, 2014). The HDACs were mounted with a thinner diamond (1.2-mm thick) on the detector side to reduce the X-ray path through the diamonds and widen the collection angle of the XAS analysis (Sanchez-Valle et al., 2004). This configuration allows i) reducing the attenuation of the fluorescence X-rays in the anvil, and ii) decreasing the fluorescence background arising from the Compton and Rayleigh scattering in the thick diamond anvils, hence increasing the signal to noise ratio and thus the overall quality of the analysis. The sample chamber, a 300-µm hole drilled in a 250-µm rhenium gasket compressed between the two diamond anvils, was heated externally with molybdenum wires wrapped around two tungsten carbide seats supporting the diamond anvils. Temperature was measured to within 2 °C with K-type thermocouples attached to each anvil, as close as possible to the sample chamber. The temperature gradient between thermocouples and the sample chamber was calibrated for each HDAC prior to experiments using the melting temperature at ambient pressure of S (115.4 °C), $NaNO_3$ (308 °C) and NaCl (800.5 °C). Overall, the *T* gradient remains < 35 °C at the highest temperature reached (850 °C).

149 Pressure was determined from the equation of state of the gold internal pressure standard
150 (Jamieson et al., 1982) whose X-ray diffraction pattern was measured during the experiment.
151
152 Partitioning experiments were conducted by loading the sample chamber with a piece of
153 Br-bearing Hpg glass and either pure H_2O or an aquous 3 wt% NaBr solution **(Fig. 1)**. For the
154 speciation measurements by XAS, loadings included either Br aqueous solutions, or a piece of
155 Br-bearing NS2 or Hpg glass loaded together with de-ionized water. In all runs, a pellet of a
156 mixture of Au and Al_2O_3 powders was added to be used for pressure calibration (Louvel et al.,
157 2013; 2014). The volumetric proportions of glass and aqueous fluid in the different loadings
158 were adjusted by adding double-side polished glass pieces of known dimensions **(Fig. 1).** Upon
159 heating, the haplogranite melt-aqueous fluid system followed the classical phase transitions
160 described in previous studies (Bureau and Keppler, 1999; Louvel et al., 2013), with initial
161 hydrous melting recorded between 550 and 700 °C **(Fig. 1B)** and complete miscibility reached
162 within the 700-850 °C range, depending on the pressure **(Fig. 1C).** In contrast, the NS2-H_2O
163 system displayed distinct and rather unusual phase relations in the investigated *P*-*T* range **(Fig.**
164 **1D-F)**: the NS2 glass first dissolved completely in the aqueous solution between 150 and 250 °C
165 to produce a single fluid phase containing 30 to 60 wt% dissolved Na_2O and SiO_2 solutes**, an**
166 **analog for slab-derived so-called supercritical fluids (Fig. 1E).** Upon further heating between
167 500 and 750 °C, the fluid unmixed into two phases, a hydrous melt and an aqueous fluid **(Fig.**
168 **1F).** This immiscibility gap remained open up to the highest temperatures reached with the
169 HDAC (800-900 °C), as also previously observed for the haploandesite $Na_2Si_4O_9$-$Na_2(Si,Al)_4O_9$
170 join and the K_2O-SiO_2-H_2O system (Mysen and Cody, 2004).

171 The composition of the high pressure fluids (wt% cations dissolved) and melts (wt% H_2O)
172 was determined from available solubility studies (Table 2) as follows. The water content of
173 haplogranite melts at equilibrium with aqueous fluids **(Fig. 1B)** was calculated from the water
174 solubility data for aluminosilicate melts reported by Mysen and Wheeler (2000) and extrapolated
175 to our experimental conditions. The composition of the aqueous fluid phase in equilibrium with
176 the haplogranite melt (*i.e.,* total silicates content including SiO_2, Al_2O_3, Na_2O and K_2O) was
177 estimated by extrapolating to the *P-T* conditions of our experiments the solubility data reported
178 for the albite-H_2O system between 0.20 and 0.84 GPa at 600 and 700 °C (Anderson and
179 Burnham, 1983), **except for Run 4, for which the high pressure (1-2 GPa) solubility data of**
180 **Wolhers et al. (2011) were employed. Uncertainties in the calculated dissolved silicate**
181 **content arise from the compositional differences between solubility models (albite) and our**
182 **experimental system (peralkaline haplogranite) but they cannot be evaluated due to a lack**
183 **of information on Si, Na, K and Al partitioning between silicate melts and water. To**
184 **account for potential uncertainties on calculated silicate contents in the fluid phase we thus**
185 **considered a 10% error on pressure conditions, which translates to an overall uncertainty**
186 **of 20-22% for all investigated conditions, except in Run 4 (Table 2).** The compositions of the
187 aqueous fluids in the NS2-H_2O system were determined from the initial volumetric proportions
188 of the NS2 glass and the aqueous fluid loaded in the compression chamber. The mass of the glass
189 was calculated from the volume using a density of 2.52(5) g/cm^3 (Yamashita et al., 2008) and
190 that of the fluid determined from the volume left in the compression chamber **(Fig. 1D).** The
191 amount of water dissolved in the hydrous NS2 melt in equilibrium with the aqueous fluid at 700
192 °C and 0.4 GPa **(Fig. 1F)** was calculated from water solubility data in sodium silicate melts

reported by Mysen and Cody (2004). The overall error in the calculated bulk compositions is within 10% of the total concentration value.

2.3 *In-situ* SXRF and XAS measurements and data analysis

The SXRF and XAS measurements were performed at the microXAS beamline (X05LA) of the Swiss Light Source (SLS, Paul Scherrer Institute, Borca et al., 2009). Measurements at the Br K-edge were conducted with an incident energy of 13.6 keV tuned by a Si(111) double crystal monochromator and focused down to 5×8 (V×H) μm^2 size by a set of Rh-coated Kirkpatrick-Baez mirrors. This configuration ensured a photon flux of 2×10^{11} photons per second at the measurements conditions. The intensity of the incident beam was monitored throughout the experiments using an Ar-filled micro-ion-chamber placed between the Kirkpatrick-Baez mirrors and the HDAC. Before measurements, temperature was stabilized for about 30 min after each heating stage to ensure that chemical equilibrium was achieved inside the cell (Louvel et al., 2014). In the case of coexisiting melt and fluid, measurements were only performed when the melt globule was stationary and bridging both diamonds **(Fig. 1F).** This configuration ensured that spectra were only collected from pure phases (fluid or melt) thus avoiding any contamination of the SXRF and XAS signals by the other coexisting phase. SXRF and XAS spectra were collected in fluorescence mode in a forward scattering geometry with an energy dispersive single-element silicon drift diode (SDD) detector (Ketek®, 139 eV resolution at Mn-K_α = 5.89 keV) set at 22° from the incident beam in the horizontal plane (Sanchez-Valle et al., 2003; Louvel et al., 2013; 2014). Angle-dispersive X-ray diffraction spectra were collected on the gold pressure calibrant before and after XAS/SXRF measurements using a high-resolution CCD

camera set in transmission geometry. A microscope equipped with a video camera was used to monitor the compression chamber during the heating and cooling cycles **(Fig. 1)**.

2D-SXRF maps were acquired across the sample chamber to qualitatively monitor the distribution of Br between the coexisting aqueous fluid and haplogranite melt (Fig. 1). Then, at least three fluorescence spectra were collected from each phase to further determine the Br fluid-melt partition coefficients $D_{Br}^{f/m}$ at each *P-T* condition (Table 2). Counting times were set to 100 or 300 s, depending on the signal intensity. **Spectra were always recorded far away from the Au pressure calibrant (Fig. 2) to suppress the contribution of the Au L_β line (11.442 keV) to the Br K_α line (11.924 keV) used for the quantifications. Note that the Au L_β line was only observed in the spectra when the beam spot was positioned within less than 5 µm away from the Au chip (horizontal beam size 8 µm) thus demonstrating the well defined beam shape and appropriate spatial resolution of the X-ray beam.**

The fluid-melt partition coefficients $D_{Br}^{f/m}$**, which correspond to the ratio of Br concentration in coexisting fluid (C_{Br}^{f}) and melt (C_{Br}^{m}) at each *P-T*,** were derived from the integrated intensities of the Br fluorescence emission lines recorded in the fluid and melt, I_f and I_m, after normalization to the incident beam intensity and counting times, and background removal with the Peakfit v4.12 software (SeaSolve Software-USA), following the method described in Louvel et al. (2014). This method relies on the fixed geometry of the HDAC set-up and takes into account the different composition, density (ϱ) and effective transmission (A) of the aqueous fluid and melt to normalize the fluorescence signal and calculate $D_{Br}^{f/m}$ according to the equation:

$$D_{Br}^{f/m} = \frac{C_{Br}^{f}}{C_{Br}^{m}} = \frac{I_f}{I_m} \times \frac{A_m}{A_f} \times \frac{\rho_m}{\rho_f} \quad (1)$$

The standard deviation on the intensity ratios I_f/I_m are smaller than 10% (Table 2). The fluid and melt densities were calculated for the relevant pressure, temperature and fluid or melt compositions using density relations determined by *in situ* techniques for comparable fluid and melt compositions by Mantegazzi et al. (2012) and Malfait et al. (2014) and taking into account the estimated uncertainties on pressure and fluid and melt compositions. The effective transmission A_f *and* A_m, which accounts for the probability that the fluorescent radiation reaches the detector depending on phase composition, density and thickness of the sample at the incident energy, were calculated from the compositionally dependent attenuation lengths λ determined below and above the Br K-edge energy as a function of melt/fluid compositions and densities for all *P-T* conditions using the Hephaestus software (Ravel and Newville, 2005). The sample thickness *t* was input as an average of the thickness of the sample chamber after each run (~ 200 μm). A variation of the sample thickness by 50 μm induces a deviation smaller than 10 % on the absolute value of the A_m/A_f ratio. The corrections in Eq. 1 significantly affect $D_{Br}^{f/m}$: because the XRF intensities correlate with the Br concentration, and the melts are denser than the fluids, the values for $D_{Br}^{f/m}$ are consistently higher than the I_f/I_m ratio (Table 2). However, total uncertainties reported on the partition coefficients mostly remain below 10 %.

XAS measurements were conducted on 3 wt% NaBr aqueous solution, 'solute-poor' fluids equilibrated with hydrous haplogranite melt **(Fig. 1B),** supercritical fluids containing different amounts of dissolved NS2 **(Fig. 1E)** and hydrous NS2 melt **(Fig. 1F).** XAS analyses on the

haplogranite melt were precluded by the lower Br concentration of these melts (< **0.2 wt%**). For each composition, 3 to 5 XAS spectra were collected with counting times of 1 second per point in the pre-edge region to 3 seconds in the XANES and EXAFS regions. The contribution of Bragg reflections arising from the diamond anvils was avoided in the energy range of interest by changing the orientation of the diamond anvil cell by 0.5 to 1° with respect to the incident X-ray beam direction (Bassett et al., 2000). The edge position was calibrated using a pellet of NaBr and no significant drift of the energy was observed during measurements. XAS spectra were also collected at ambient conditions on ~ 200×200 μm^2 double-side polished section of the NS2 and Hpg glasses.

Data reduction was performed using the Athena and Artemis packages (Ravel and Newville, 2005) based on the IFEFFIT program (Newville, 2001). Averaged experimental spectra were normalized to the absorption edge height and background removed using the automatic background subtraction routine AUTOBK included in the Athena software. To minimize the contribution of features at distances below the atom-atom contact distance, the R_{bkg} parameter, which represents the minimum distance for which information is provided by the signal, was set to 1.3 Å. For all spectra, the absorption energy E_0 was set to 13.474 keV, which corresponds to the maximum of the first derivative of the absorption edge. Based on previous studies of Br and Cl speciation in aqueous solutions and silicate glasses (Ayala et al., 2002; D'Angelo et al., 1993; Evans et al., 2008; Ferlat et al., 2001; McKeown et al., 2011; Ramos et al., 2000; Sandland et al., 2004; Stebbins and Du, 2002), our EXAFS analysis included the Br-O and Br-Na scattering paths to describe the evolution of the local structure around Br from the high *P-T* fluids to the hydrous melts and silicate glasses. Although Na cannot be easily distinguished from Al or Si by EXAFS under our experimental conditions, the presence of

network cations in the nearest coordination shell of Br is deemed unlikely, as shown for Cl by MAS-NMR and XAS studies (Evans et al., 2008; McKeown et al., 2011; Sandland et al., 2004; Stebbins and Du, 2002). The theoretical back-scattering amplitudes, mean free-paths and phase-shift functions for these paths were calculated with the FEFF6.0 *ab initio* code (Mustre de Leon et al., 1991) using an aqueous Br ion $[Br(H_2O)_6]^-$ with a mean Br-O distance of 3.37 Å and the NaBr salt crystallographic structure with a Br-Na distance of 2.98 Å (Deshpande, 1961; Makino, 1995). Multiple scattering within a linear Br···H-O cluster was also included to model the hydration shell around Br, with the H-O distance fixed to 1.0 Å (Silvestrelli and Parrinello, 1999; Soper and Benmore, 2008). The $\chi(k)$ EXAFS function were Fourier filtered over the 1.5-6.0 $Å^{-1}$ *k*-range for most spectra. For all samples, modelling of the EXAFS oscillations was performed using 4 variables: average coordination number (N), distance to nearest neighbor (R), Debye-Waller factor σ^2, and the energy shift ΔE (which is a non-structural parameter). The amplitude reduction factor S_0^2 was set to 1 based on previous fits of aqueous NaBr, KBr and $GaBr_3$ solutions (Da Silva et al., 2009; Ferlat et al., 2002). All fits were performed simultaneously with k-weighting of 1, 2 and 3 in order to decrease correlations between N and σ^2, and R and ΔE (Pokrovski et al., 2009a,b). The multi-electronic excitations (MEE) at 34 and 90 (± 1) eV above the Br K-edge (D'Angelo et al., 1993) were neglected as they did not significantly contribute to the EXAFS spectra. The variation of ΔE values between different fitted samples was less than ± 4 eV, further confirming the validity of the fitting procedure and the accuracy of the derived interatomic distances.

3 RESULTS AND DISCUSSION

3.1 Bromine partition coefficients in the haplogranite-fluid system

306 The distribution of Br between aqueous fluids and silicate melts at high *P-T* conditions
307 has been constrained by measuring fluid-melt partition coefficients $D_{Br}^{f/m}$ from 592 to 840 °C
308 and from 0.2 to 1.7 GPa in four experimental runs. For all investigated conditions, the $D_{Br}^{f/m}$
309 values are always higher than 1 (Table 2), confirming the preferential partitioning of Br into the
310 fluid phase, which is also qualitatively evident from the *in-situ* Br distribution maps reported in
311 **Figure 2**. The $D_{Br}^{f/m}$ values vary between 2.0 ±0.1 and 15.3 ±1.0, and fall within the range
312 reported in a previous HDAC study by Bureau et al. (2010) at similar *P-T* conditions **(Fig. 3).**
313 **Our limited set of $D_{Br}^{f/m}$ values does not show any pressure, composition or density**
314 **dependence as it may generally be expected for vapor-liquid and fluid-melt equilibrium**
315 **partitioning of elements, which postulates that a partition coefficient should tend to 1 when**
316 **approaching the critical point at which the compositions and densities of both phases are**
317 **identical by definition (e.g., Bureau and Keppler, 1999; Pokrovski et al., 2013 and**
318 **references therein). However, previous vapor-liquid partitioning studies for base metals**
319 **(Cu, Au) demonstrated that large differences between the chemical speciation in the vapor**
320 **and liquid phase may obscure simple density-dependent partitioning trends (e.g.,**
321 **Pokrovski et al., 2008). By analogy, it may be expected that if Br speciation is significantly**
322 **different in the coexisting melt and fluid (see section 3.2), partitioning trends versus bulk**
323 **system parameters such as water activity, density or pressure may not be straighforward.**
324 **This is likely the case for previous high *P-T* measurements of $D_{Br}^{f/m}$ (Bureau et al., 2010)**
325 **that do not show clear *P*-dependence at least within the high *P*-range investigated (> 0.6**
326 **GPa) .**

Additionally, the apparent lack of pressure dependence of the $D_{Br}^{f/m}$ in our study may also reflect uncertainties in the calculated fluid and melt composition that translate to the calculated $D_{Br}^{f/m}$ (section 2.1 and 2.3). In this regard, the large $D_{Br}^{f/m}$ = 9.7 obtained at 1.7 GPa in Run 4, when the system should be close to miscibility and $D_{Br}^{f/m}$ ~ 1, is striking (Table 2, Fig. 3). This deviation from 1 may result, at least partly, from the different method employed to compute fluid composition for this run (high *P* solubility data from Wohlers et al., 2011) or from non-Henrian behavior of Br in this system (*i.e.,* ~ 2 wt% Br dissolved in the sample chamber compared to only 0.5 - 0.6 wt% for Runs 1 to 3).

Despite those uncertainties, an important finding here is that the $D_{Br}^{f/m}$ values remain relatively small **(< 15) under high *P-T* conditions. Assuming that the high *P-T* fluid/melt volumetric ratio is similar to the initial fluid/glass ratio for each run, we calculate between 400 to almost 2000 ppm Br (0.04-0.2 wt%) dissolved in the high *P-T* hydrous melts at run conditions.** This observation suggests that hydrous granitic melts have a capacity comparable to fluids to carry Br under high *P-T* conditions and may thus contribute to the efficient transport and recycling of Br from the subducting slab to the mantle wedge and volcanic arc.

At low-pressure conditions relevant to fore-arc or crustal processes (< 0.2 GPa), our *in-situ* partition coefficients are slightly lower than those obtained from quench experiments **(Fig. 3).** For instance, Bureau et al. (2000) and Cadoux et al. (2018) reported average $D_{Br}^{f/m}$ of ~ 17-20 for albitic and rhyodacitic melts at 900 °C and 0.2 GPa, while we found $D_{Br}^{f/m}$ of ~ 5 at 800 °C and 0.2 GPa. We also note that the minimum $D_{Br}^{f/m}$ value from Cadoux et al. is ~ 9, which is closer to our *in-situ* value. These rather small variations may stem from uncertainties in the

pressure determination below 0.5 GPa in the HDAC, the quantification of Br by mass balance in Bureau et al. and Cadoux et al. (i.e, salt precipitates), or artifacts of the quench method resulting in the loss of Br to the aqueous phase upon cooling. Furthermore, slight differences in the melt composition and structure could also result in different Br speciation (Louvel et al., 2020), favoring or not the incorporation of Br in the silicate melt. **The relatively low Br partition coefficients (< 20) compare favorably with those reported for Cl for silicic compositions, confirming the similar behavior of Br and Cl under magmatic conditions. Indeed, fluid-melt partition coefficients from experiments with low Cl concentration (< 1m Cl) range between ~ 3 and 20 for phonolitic to rhyolitic composition (Chevychelov et al., 2008; Webster and Holloway, 1988; see Dolejs and Zajacz, 2018 for a review). Together, these experimental results confirm natural observations that felsic magmas may retain high amounts of Cl and Br, especially if they are subjected to fast decompression (Balcone-Boissard et al., 2010).**

3.2 Speciation of bromine in aqueous fluids and silicate melts

3.2.1 Aqueous solutions and silicate glasses at room conditions

The XANES and EXAFS spectra collected at ambient conditions from the 3 wt% NaBr aqueous solution and Br-bearing silicate glasses are reported respectively **in Fig. 4 and Fig. 5**, together with data for a KBr aqueous solution from Ferlat et al. (2002). These spectra were employed to validate the theoretical backscattering amplitude and phase shift functions for Br-O and Br-Na scattering paths used in EXAFS modeling. The XANES spectrum of the 3 wt% NaBr aqueous solution is characterized by an absorption edge at 13.474 keV and a white line that peaks at 13.478 keV **(Fig. 4).** It displays close similarities to that of the KBr aqueous solution

372 from Ferlat et al. (2002) and overall resembles other alkali bromide aqueous solutions reported in
373 the literature (Wallen et al., 1997; Ferlat et al., 2001; Evans et al., 2007). The EXAFS spectra
374 from the KBr and NaBr aqueous solutions are accurately modeled with a hydration shell of 5.7 ±
375 0.8 and 5.9 ± 0.7 water molecules ($N_{Br..H-O}$) at a Br-O distance of 3.30 ± 0.03 and 3.37 ± 0.04 Å,
376 respectively (Table 3). Note that multiple-scattering paths from the linear Br···H-O cluster are
377 needed to accurately reproduce the experimental data; when only Br-O interactions are
378 considered, the model fails to reproduce the amplitude of the EXAFS oscillations unless an
379 unrealistic hydration shell of ~12 H_2O molecules is adopted. The structural parameters fitted for
380 the KBr aqueous solution from Ferlat et al. (2002) are, within errors, similar to those reported by
381 the authors. Together with the EXAFS fits of the NaBr aqueous solution, they confirm that Br
382 speciation in aqueous solution at room conditions is dominated by a six-fold coordinated
383 hydration shell with the H-O bond of the water molecule radially aligned towards the Br ion
384 (Ferlat et al., 2001; Ramos et al., 2000).

385 EXAFS spectra collected on NS2 and Hgp glasses at room conditions display distinct
386 oscillations, with a new feature at 2.2 $Å^{-1}$ in both glass samples and amplitudes nearly out of
387 phase at > 2 $Å^{-1}$ in *k*-space compared to the NaBr and KBr aqueous solutions **(Fig. 6).** Different
388 combinations of Br-Na and Br-O scattering paths were tested to constrain the local structural
389 environment of Br in the silicate glasses. Models considering individually either the Br-Na or Br-
390 O paths do not provide a reasonable fit of the EXAFS oscillations and the simultaneous
391 contribution of Br-Na and Br-O bond is required to reproduce the experimental spectra. The
392 EXAFS-derived parameters suggest that Br in NS2 and Hpg glasses is coordinated to an average
393 of 6 Na cations in the first shell at an average distance of 2.95 Å, and next-nearest 6 O neighbors
394 located at 3.4 Å (Table 3). The fitted Br-Na bond length is consistent, within errors, with

theoretical Br-Na distances in crystalline NaBr (2.987 Å, Deshpande, 1961) and is close to that reported for aluminosilicate glasses in a previous study (Cochain et al., 2015), suggesting Br is incorporated in the silicate glasses in a "salt-like" structure, similar to NaBr. The similarities between the structural parameters fitted for anhydrous NS2 and hydrous Hpg (3.3 wt% H_2O) glasses also suggest that the nearest environment of Br remains largely anhydrous in glasses containing relatively low water contents and that the second O neighbors may be from the silicate network rather than more distant H_2O or OH groups. Attempts to include the effect of Br···H-O bonds in the fitting model by taking into account multiple scattering Br···H-O paths instead of Br-O correlations only resulted in a systematic decrease in the fit quality (higher *R*-factor). The sole difference between the two glasses is the presence of a pre-edge feature at ~13.468 keV in the haplogranite glass **(Fig. 5).** Such features have been attributed to the 1s to 4p electronic transitions in Br (Burattini et al., 1991) and reported in several covalently bonded and/or reduced Br-bearing compounds, including HBr, Br_2, and $CHBr_3$ (D'Angelo et al., 1993; Feiters et al., 2005). While Evans et al. (2007) suggested that this feature could arise from partial Br reduction in the presence of remaining carbon material in the sample from the synthesis, changes in the local site symmetry around Br could also contribute to the development of such feature. Recent HERFD-XAS measurements conducted on silicate glasses however demonstrate that this feature is absent in basaltic and andesitic glasses and hence, may be specific to the structure of granitic glass compositions (Louvel et al., 2020).

3.2.2 High *P-T* aqueous fluids and hydrous silicate melts

Bromine K-edge XANES spectra of high *P-T* aqueous fluids (3 wt% NaBr solution, fluids at equilibrium with haplogranite melt and water-dominated fluids containing < 50 wt%

418 dissolved NS2) all share a shape very similar to that of the NaBr aqueous solution at room
419 conditions, suggesting a similar local structure of Br in H_2O-dominated phases at elevated *P-T*
420 **(Fig. 4 and 5).** Differences in the shape of the XANES spectra become more pronounced for the
421 supercritical fluids with >50 wt% dissolved Si and Na and the hydrous NS2 melt **(Fig. 4).**
422 Although the maximum of the white line remains at 13.478 keV, it broadens and decreases in
423 amplitude compared to the 3 wt% NaBr aqueous solution. Also, the first post-edge resonance is
424 shifted toward either higher (13.504 keV) or lower (13.487 keV) energies compared to the
425 aqueous fluids. These changes may be indicative of the progressive incorporation of Na in the
426 local structure around Br. These modifications of Br coordination environment are also
427 noticeable in the EXAFS oscillations **(Fig. 5):** while Br-bearing aqueous fluids mostly show a
428 decrease of the amplitude of the oscillations with increasing *P-T*, they are shifted to higher
429 distances (*i.e.* from 2.6 to 2.8 $Å^{-1}$ in *k*-space for the first oscillation) for the 60 wt% NS2 fluid.
430 Moreover, the NS2 melt bears closer resemblance to the NS2 and Hpg glasses, sharing similar
431 oscillations at 2.2 and 3.2 $Å^{-1}$.

432 The structural parameters derived from the quantitative EXAFS analysis are reported in
433 Table 4. Comparably to room conditions, the EXAFS spectra of the NaBr aqueous solution at
434 high pressure-temperature conditions are well matched by an octahedral hydration shell
435 including multiple-scattering contributions from the Br···H-O cluster **(Fig. 6).** Br-O coordination
436 numbers and distances are, respectively, 6.4 ± 1.1 and 3.40 ± 0.07 Å at 450 °C and 0.6 GPa,
437 indicating the persistence of the 6-fold coordinated hydration shell up to high temperatures. This
438 observation contrasts with results from a number of classical EXAFS studies performed at lower
439 pressures (< 0.07 GPa at 450 ºC) that reported significant reduction in the number of water
440 molecules around Br at supercritical conditions (Wallen et al., 1997; Da Silva et al., 2009). These

differences are likely to reflect the differences in pressure (or fluid density), with higher pressures stabilizing the hydration shell around Br due to the increase in the solvent dielectric constant (Pan et al., 2013; Sverjensky et al., 2014), as also predicted for other ions such as Li^+ (Jahn and Wunder, 2009) and Ti^{4+} (van Sijl et al., 2010) by molecular dynamics simulations. An exception to this trend are the experimental results of Mayanovic et al. (2001), who reported a decrease by > 60% of the number of water molecules in the solvation shell of both Br aqua ions and $ZnBr_4^{2-}$ complexes in 1 m $ZnBr_2$ - 6 m NaBr aqueous solution from ambient conditions to 500 ºC and 0.5 GPa. The reason for this discrepancy is unclear at this state of our knowledge and additional studies on the speciation of Br in aqueous electrolytes will be necessary to explain the disagreement.

There are no significant changes in Br speciation in the aqueous fluids equilibrated with haplogranitic melts, which contain only few wt% of dissolved silicate components, and in fluids containing up to 30 wt% dissolved NS2 (**Fig. 6**; Table 4). The first noticeable changes are only found for fluids containing at least 50 wt% dissolved NS2, with a small decrease of the average Br coordination number ($N_{Br\ldots H\text{-}O}$) to ~ 4.7 compared to more dilute fluids (~ 6.0). While this value stays within errors from the other compositions, the reduction of the hydration shell might define the onset of Br-Na complexation with increasing amount of Na dissolved in the fluid. This hypothesis was tested by introducing a Br-Na contribution in the fitting model for the high temperature data, but this resulted in a decrease of the overall fit quality. The formation of Br-Na complexes and the partial dehydration of Br, however, becomes evident with further increase of the solute content to 60 wt% dissolved NS2 in the fluid (Table 4). For this composition, the best-fit model is consistent with the presence of ~ 3 Na atoms and 4 to 5 H_2O molecules (or OH groups) in the nearest environment of Br, at 480 °C and 1.5 GPa and 610 ºC and 2.2 GPa. In the

464 NS2 hydrous melt (10 wt% H_2O), the number of Na neighbors further increases to ~ 6 whereas
465 the number of oxygens remains similar to that of the 60 wt% NS2 fluid (~ 3.4). This increase in
466 the number of Na neighbors compared to the 60 wt% NS2-bearing fluid suggests that the nearest
467 environment of Br in silicate-rich fluids progressively approaches the local structure observed in
468 the NS2 glass. Yet, the Br local environement remains hydrated, in contrast to the NS2 and Hpg
469 glasses. Based on results from FTIR and ^{29}Si NMR studies showing that molecular H_2O is
470 favored in aluminosilicate and sodium silicate glasses as the amount of dissolved water increases
471 (Stolper, 1982; Uchino et al., 1992; Xue and Kanzaki, 2004; Behrens and Yamashita, 2008), we
472 suggest that molecular H_2O, rather than OH groups, would be present around Br in the hydrous
473 NS2 melt. Moreover, we cannot exclude that distinct "fluid-like" $Br(H_2O)_6$ and "glass-like"
474 $BrNa_6$ complexes coexist in the hydrous melt as $[yBr(H_2O)_6 + xBrNa_6]$ moieties, as the average
475 signal of these structures could not be distinguished from $[BrNa_y(H_2O)_x]$ clusters by XANES or
476 EXAFS. **Although Br speciation could not be investigated in the hydrous haplogranite melt**
477 **due to lower Br concentrations (< 0.2 wt%), the similarities between both XANES and**
478 **EXAFS spectra of the Hpg and NS2 glasses (Fig. 4 and 5) allow us to anticipate a similar Br**
479 **local environment in the haplogranite melt, dominated by alkali complexation.**
480

481 **4 Implications for the transport and recycling of halogens in subduction zones**

482 The new partitioning and speciation data derived for bromine in the present study provide
483 direct insights on the recycling and transport mechanisms of halogens (Cl, Br and I) in
484 subduction zones. Our results suggest that the mobilization of Br (and likely Cl, Br and I) in
485 subduction zones is affected by the chemistry of the slab-derived mobile phases. These phases, in
486 turn, are essentially controlled by the slab composition and the depth of fluid extraction and

hence, by the *P-T* conditions (Schmidt and Poli, 1998; Manning, 2004; Schmidt et al., 2004; Hermann et al., 2006; Bebout, 2007; Keppler, 2017). Figure 6 illustrates a gradual transition of Br speciation from hydrated species $[Br(H_2O)_6]^-$ to $[BrNa_x(H_2O)_y]$ clusters with various stoichiometries (or mixture of $[Br(H_2O)_6]$ and $BrNa_6$ moieties) as the fluid composition evolves from diluted aqueous fluids such as those released by continuous metamorphic dehydration of the slab (< 15 wt% dissolved solutes, Manning, 2004; Rustioni et al., 2019) to Si/Na-rich supercritical fluids that form owing to enhanced solubility of silicate minerals at depth and/or granitic melts produced by fluid-assisted melting of subducted sediments (Hermann et al., 2006; Skora and Blundy, 2010). The increasing similarities in the local structure of Br in aqueous fluids containing large amounts of dissolved alkali-silica (> 12.5 wt% Na) and the hydrous melts **(Fig. 6)** is consistent with the progressive decrease in the Br fluid-melt partition coefficients ($D_{Br}^{f/m}$) with *T* increase observed in this study **in each separated runs (Fig. 3).** Sodium complexation with Br is thus an efficient mechanism that enables not only aqueous fluids but also supercritical fluids and hydrous melts to carry significant amounts of Br at depth.

General similarities between Cl, Br and I speciation in aqueous solutions and silicate glasses (Evans et al., 2008; McKeown et al., 2011,2015; Shermann et al., 2010) suggest that the speciation and partitioning trends found in our study for Br may extend to Cl and I. Therefore, while early dehydration fluids should release large amounts of halogens to the fore-arc and the mantle wedge (100 – 200 km depth), hydrous slab melts and supercritical fluids play a critical role in recycling the residual halogens dragged by the subducting slabs to greater depths. Such efficient recycling, where most of the Cl and Br subducted is transfered to the mantle wedge and ultimately returned to the surface through arc magmatism, is further supported by recent quantification of halogens in subducted sediments, serpentinites and altered oceanic crust. Mass

balance calculations indeed show a close match between worldwide influx to the mantle wedge, ~ 13-15 $\times 10^3$ kt/yr Cl and 5-70 kt/yr Br, and calculated outflux as HCl and HBr at volcanic arcs, ~ 3-22 $\times 10^3$ kt/yr Cl and 5-15 kt/yr Br. (Barnes et al., 2018; Chavrit et al., 2016; Kendrick et al., 2013; Pyle and Mather, 2009). In comparison, iodine degassing at volcanic arcs is less well constrained, making it more difficult to assess its fate in the subduction factory (e.g., Bureau et al., 2016). The small imbalances remaining between Cl and Br input and output fluxes may arise from difficulties in quantifying halogen loss to the fore-arc and crustal hydrothermal systems. Recent reports of halogens enrichment in oceanic islands basalts (Barnes et al., 2018; Hanyu et al., 2019; Kendrick et al., 2017) also point to the subduction of a noticeable fraction of F, Cl, Br and I to greater depth, to an extent that is yet to be quantified.

5. Conclusions

In-situ SXRF and XAS have been applied to quantify Br fluid-melt partition coefficients and speciation in aqueous fluids, supercritical fluids and hydrous silicate melts up to 840 °C and 2.2 GPa. Above all, our experimental results demonstrate how changes in speciation, from hydrated ions in aqueous fluids to 'salt-like' structures in hydrous melts, may facilitate the uptake of high amounts of Cl, Br and probably I by subduction zone fluids, regardless of their composition. Significant efforts are however still needed to accurately quantify halogen cycling from the surface to the deep Earth and back. Especially, new experiments investigating the solubility of halogens in subduction zone fluids and the capacity of high-pressure minerals (e.g., micas, Ti-clinohumite, apatite, and carbonates) to incorporate these elements are still necessary

to evaluate the amounts of halogen that may be returned to the volcanic arc or retained in the slab.

Acknowledgements: This work was supported by the Swiss National Science Foundation (grants 200021-120575 and 200020-132208 to CSV) and by the Swiss Academy of Sciences (SATW) and the Ministères des Affaires étrangères et européennes (MAEE) et de l'Enseignement Supérieur et de la Recherche (MESR) through the Partenariat Hubert Curien (PHC). We thank M. Doebeli and J. H. Seo for conducting the RBS and LA-ICPMS analysis, respectively. The Paul Scherrer Institute (PSI) and the Swiss Light Source (SLS) are acknowledged for providing beamtime for the experiments. **Two anonymous reviewers helped to improve the original manuscript.**

References

Anderson, G. M. and Burnham, C. W., 1983. Feldspar solubility and the transport of aluminum under metamorphic conditions. Am. J. Sci. 283, 283-297.

Aranovich, L.Y. and Newton, R.C., 1996. H_2O activity in concentrated NaCl solutions at high pressures and temperatures measured by the brucite-periclase equilibrium. Contrib. Mineral. Petr. 125, 200-212.

Ayala, R., Martinez, J. M., Pappalardo, R. R., Saint-Martin, H., Ortega-Blake I. and Sanchez-Marcos, E., 2002. Development of first-principles interaction model potentials. An application to the study of the bromide hydration. J. Chem. Phys. **117**, 10512.

554 Baasner, A., Hung, I., Kemp, T.F., Dupree, R., Schmidt, B.C. and Webb, S.L., 2014. Constraints on the
555 incorporation mechanism of chlorine in peralkaline and peraluminous Na_2O-CaO-Al_2O_3-SiO_2
556 glasses. Am. Mineral. 99, 1713-1723.
557 Balcone-Boissard, H., Villemant, B., and Boudon, G., 2010. Behavior of halogens during the degassing of
558 felsic magmas. Geochem. Geophy. Geos. **11**.
559 Barnes, J., Manning, C.E., Scambelluri, M. and Selverstone, J., 2018. The behaviour of halogens during
560 subduction-zone processes. In D.E. Harlov and L. Aranovich (eds.), The Role of Halogens in
561 Terrestrial and Extraterrestrial Geochemical Processes, Springer Geochemistry, 545-590.
562 Bassett, W. A., Shen, A. H., Bucknum, M., and Chou, I. M., 1993. A New Diamond-Anvil Cell for
563 Hydrothermal Studies to 2.5 GPa and from – 190 °C to 1200 °C. Rev. Sci. Instrum. 64, 2340-2345.
564 Bassett, W. A., Anderson, A. J., Mayanovic, R. A., and Chou, I.-M., 2000. Hydrothermal diamond anvil
565 cell for XAFS studies of first-row transition elements in aqueous solution up to supercritical
566 conditions. Chem. Geol. **167**, 3-10.
567 Bebout, G. E., 2007. Metamorphic chemical geodynamics of subduction zones. Earth Planet. Sc. Lett.
568 **260**, 373-393.
569 Behrens, H. and Yamashita, S., 2008. Water speciation in hydrous sodium tetrasilicate and hexasilicate
570 melts: Constraint from high temperature NIR spectroscopy. Chem. Geol. **256**, 306-315.
571 Bergstrom, P-A. and Lindgren, J., 1991. An IR study of the hydration of ClO_4^-, NO_3^-, I^-, Br^-, Cl^- and SO_4^{2-}
572 anions in aqueous solution. J. Phys. Chem. 95, 8575-8580.
573 Bobrowski, N., Honninger, G., Galle, B., and Platt, U., 2003. Detection of bromine monoxide in a
574 volcanic plume. Nature 423, 273-276.
575 Borca, C. N., Grolimund, D., Willimann, M., Meyer, B., Jefimovs, K., Vila-Comamala, J., and David, C.,
576 2009. The microXASbeamline at the Swiss Light Source: towards nano-scale imaging. J. Phys.
577 Conf. Ser. 186, 1-3.
578 Borchert, M., Wilke, M., Schmidt, C., and Rickers, K., 2009.Partitioning and equilibration of Rb and Sr
579 between silicate melts and aqueous fluids. Chem. Geol. 259, 39-47.

580 Burattini, E., D'Angelo, P., Giglio, E. and Pavel, N.V., 1991. EXAFS study of probe molecules in
581 micellar solutions. J. Phys. Chem. 95, 7880-7886.
582 Bureau, H. and Keppler, H., 1999. Complete miscibility between silicate melts and hydrous fluids in the
583 upper mantle: experimental evidence and geochemical implications. Earth Planet. Sc. Lett. 165,
584 187-196.
585 Bureau, H. and Métrich, N., 2003. An experimental study of bromine behaviour in water-saturated silicic
586 melts. Geochim. Cosmochim. Ac. 67, 1689-1697.
587 Bureau, H., Keppler, H., and Metrich, N., 2000. Volcanic degassing of bromine and iodine: experimental
588 fluid/melt partitioning data and applications to stratospheric chemistry. Earth Planet. Sc. Lett. 183,
589 51-60.
590 Bureau, H., Foy, E., Raepsaet, C., Somogyi, A., Munsch, P., Simon, G., and Kubsky, S., 2010. Bromine
591 cycle in subduction zones through in situ Br monitoring in diamond anvil cells. Geochim.
592 Cosmochim. Ac. 74, 3839-3850.
593 Bureau, H., Auzende A-L., Marocchi, M., Raepsaet, C., Munsch, P., Testemale, D., Mezouar, M.,
594 Kubsky, S., Carriere, M., Ricolleau, A. and Fiquet, G., 2016. Modern and past volcanic degassing
595 of iodine. Geochim. Cosmochim. Ac. 173, 114-125.
596 Cadoux, A., Iacono-Marziano, G., Scaillet, B., Aiuppa, A., Mather, T.A., Pyle, D.M., Deloule, E.,
597 Gennaro, E. and Paonita, A., 2018. The role of melt composition on aqueous fluid vs. silicate melt
598 partitioning of bromine in magmas. Earth Planet. Sc. Lett. 498, 450-463.
599 Carroll, M. R., 2005. Chlorine solubility in evolved alkaline magmas. Annals of Geophysics 48, 619-631.
600 Carroll, M. R. and Webster, J. D., 1994. Solubilities of sulphur, noble gases, nitrogen, chlorine and
601 fluorine in magmas. Rev. Mineral. Geochem. 30, 231-279.
602 Chavrit, D., Burgess, R., Sumino, H., Teagle, D.A.H., Droop, G., Shimizu, A. and Ballentine, C.J., 2016.
603 The contribution of the hydrothermal alteration of the ocean crust to the deep halogen and noble
604 gas cycles. Geochim. Cosmochim. Ac. 183, 106-124.

605 Chevychelov, V.Y., Botcharnikov, R.E. and Holtz, F., 2008. Partitioning of Cl nd F between fluid and
606 hydrous phonolitic melt of Mt. Vesuvius at ~850-1000 °C and 200 MPa. Chem. Geol. 256, 172-
607 184.
608 Chu, W. K. and Liu, J. R., 1996. Rutherford backscattering spectrometry: Reminiscences and progresses.
609 Mat. Chem. Phys. 46, 183-188.
610 Cochain, B., Sanloup, C., de Grouchy, C., Crepisson, C., Bureau, H., Leroy, C., Kantor, I., Irifune, T.,
611 2015. Bromine speciation in hydrous silicate melts at high pressure. Chem. Geol. 404, 18-26.
612 Dalou, C., Mysen, B.O. and Foustoukos, D., 2015. In-situ measurements of fluorine and chlorine
613 speciation and partitioning between melts and aqueous fluids in the Na_2O-Al_2O_3-SiO_2-H_2O system.
614 Am. Mineral. 100, 47-58.
615 D'angelo, P., Dicicco, A., Filipponi, A., and Pavel, N. V., 1993. Double-electron excitation channels at th
616 Br K-edge of HBr and Br_2. Phys. Rev. A 47, 2055-2063.
617 Da Silva, C., Proux, O., Hazemann, J. L., James-Smith, J., Testemale, D., and Yamaguchi, T., 2009. X-
618 ray absorption spectroscopy study of solvation and ion-pairing in aqueous gallium bromide
619 solutions at supercritical conditions. J. Mol. Liq. 147, 83-95.
620 Deshpande, V., 1961. Thermal Expansion of Sodium Fluoride and Sodium Bromide. Acta Crystallogr.
621 14, 794.
622 Dolejs, D. and Zajacz, Z., 2018. Halogens in silicic magmas and their hydrothermal systems. In D.E.
623 Harlov and L. Aranovich (eds.), The Role of Halogens in Terrestrial and Extraterrestrial
624 Geochemical Processes, Springer Geochemistry, 431-543.
625 Evans, K. A., Mavrogenes, J., and Newville, M., 2007. The effect of CO_2 on the speciation of bromine in
626 low-temperature geological solutions: an XANES study. J. Synchrotron Radiat. 14, 219-226.
627 Evans, K. A., Mavrogenes, J. A., O'Neill, H. S., Keller, N. S., and Jang, L. Y., 2008. A preliminary
628 investigation of chlorine XANES in silicate glasses. Geochem. Geophy. Geosy. 9. Q10003,
629 doi:10.1029/2008GC002157.

630 Evans, K.A., Gordon, R.A., Mavrogenes, J.A. and Tailby, N., 2009. The effect of CO_2 on the speciation
631 of RbBr in solution at temperatures to 579 °C and pressures to 0.26 GPa. Geochim. Cosmochim.
632 Ac. 73, 2631-2644.
633 Feldman, L. C. and Mayer, J. W., 1986. Fundamentals of Surface and Thin Film Analysis. Prentice Hall.
634 pp 352.
635 Ferlat, G., San Miguel, A., Jal, J. F., Soetens, J. C., Bopp, P. A., Daniel, I., Guillot, S., Hazeman, J. L.,
636 and Argoud, R., 2001. Hydration of the bromine ion in a supercritical 1 : 1 aqueous electrolyte.
637 Phys. Rev. B 63.
638 Ferlat, G., San Miguel, A., Jal, J. F., Soetens, J. C., Bopp, P. A., Hazemann, J. L., Testemale, D., and
639 Daniel, I., 2002. The quest for ion pairing in supercritical aqueous electrolytes. J. Mol. Liq. 101,
640 127-136.
641 Frezzotti, M.L. and Ferrando, S., 2015. The chemical behavior of fluids released during deep subduction
642 based on fluid inclusions. Am. Mineral. 100, 352-377.
643 Fulton, J. L., Chen, Y., Heald, S.M. and Balasubramanian, M., 2006. Hydration and contact ion pairing of
644 Ca2+ with Cl- in supercritical aqueous solution. J. Chem. Phys. 125, 094507-1-10.
645 Fulton, J. L., Schenter, G. K., Baer, M. D., Mundy, C. J., Dang, L. X., and Balasubramanian, M., 2010.
646 Probing the Hydration Structure of Polarizable Halides: A Multi-edge XAFS and Molecular
647 Dynamics Study of the Iodide Anion. J. Phys. Chem. B 114, 12926-12937.
648 Grutzner, T., Klemme, S., Rohrbach, A., Gervasoni, F. and Berndt, J., 2017. The role of F-clinohumite in
649 volatiles recycling processes in subduction zones. Geology 45, 443-446.
650 Hanyu, T., Shimizu, K., Ushikubo, T., Kimura, J-I., Chang, Q., Hamada, M., Ito, M., Iwamori, H. and
651 Ishikawa, T., 2019. Tiny droplets of ocean island basalts unveil Earth's deep chlorine cycle. Nat.
652 Commun. 10:60. https://doi.org/10.1038/s41467-018-07955-8.
653 Heinrich, C. A., Pettke, T., Halter, W. E., Aigner-Torres, M., Audétat, A., Günther, D., Hattendorf, B.,
654 Bleiner, D., Guillong, M., and Horn, I., 2003. Quantitative multi-element analysis of minerals, fluid

655 and melt inclusions by laser-ablation inductively-coupled-plasma mass-spectrometry. Geochim.
656 Cosmochim. Ac. 67, 3473-3497.
657 Hermann, J., Spandler, C., Hack, A. and Korsakov, A.V., 2006. Aqueous fluids and hydrous melts in
658 high-pressure and ultra-high pressure rocks: Implications for element transfer in subduction zones.
659 Lithos 92, 399-417.
660 Ikemoto, A. and Iwamori, H., 2014. Numerical modeling of trace element transportation in subduction
661 zones : implications for geofluid processes. Earth Planets Space 66:26, 1-10.
662 Jahn, S. and Wunder, B., 2009. Lithium speciation in aqueous fluids at high P and T studied by ab initio
663 molecular dynamics and consequences for Li-isotope fractionation between minerals and fluids.
664 Geochim. Cosmochim. Ac. 73, 5428-5434.
665 Jamieson, J. C., Fritz, J. N., and Manghnani, M. H., 1982. Pressure measurement at high temperature in
666 X-ray diffraction studies: gold as a primary standard in High-Pressure Research in Geophysics, pp
667 27-48. Center for Academic Publishing, Tokyo.
668 John, T., Scambelluri, M., Frische, M., Barnes, J. D., and Bach, W., 2011. Dehydration of subducting
669 serpentinite: Implications for halogen mobility in subduction zones and the deep halogen cycle.
670 Earth Planet. Sc. Lett. 308, 65-76.
671 Kendrick, M.A., Honda, M., Pettke, T., Scambelluri, M., Phillips, D. and Giuliani, A., 2013. Subduction
672 zone fluxes of halogens and noble gases in seafloor and forearc serpentinites. Earth Planet. Sc. Lett.
673 365, 86-96.
674 Kendrick, M.A., Jackson, M.G., Kent, A.J., Hauri, E.H., Wallace, P.J. and Woodhead, J., 2014.
675 Contrasting behaviours of CO_2, S, H_2O and halogens (F, Cl, Br, and I) in enriched-mantle melts
676 from Pitcairn and Society seamounts. Chem. Geol. 370, 69–81.
677 Kendrick, M.A., Honda, M. and Vanko, D.A., 2015. Halogens and noble gases in Mathematician Ridge
678 meta-gabbros, NE Pacific: implication for oceanic hyrothermal root zones and global volatile
679 cycles. Contrib. Mineral. Petr. 170:43.

680 Kendrick, M.A., Hemond, C., Kamenetsky, V.S., Danyushevsky, L., Devey, C.W., Rodemann, T.,
681 Jackson, M.G. and Perfit, M.R., 2017. Seawater cycled throughout Earth's mantle in partially
682 serpentinized lithosphere. Nat. Geosci. 10, 222-229.
683 Kendrick, M.A., Scambelluri, M., Hermann, J. and Padron-Navarta, J.A., 2018. Halogens and noble gases
684 in serpentinites and secondary peroditites: Implications for seawater subduction and the origin of
685 mantle neon. Geochim. Cosmochim. Ac. 235, 285-304.
686 Keppler, H., 2017. Fluids and trace element transport in subduction zones. Am. Mineral. 102, 5-20.
687 Kimura, J-I., Gill, J-B., Skora, S., van Keken, P.E. and Kawabata, H., 2016. Origin of geochemical
688 mantle components: Role of subduction filter. Geochem. Geophy. Geosy. 17, 3289-3325.
689 Louvel, M., Sanchez-Valle, C., Malfait, W.J., Testemale, D. and Hazemann, J-L., 2013. Zr complexation
690 in high pressure fluids and implications for the mobilization of HFSE in subduction zones.
691 Geochim. Cosmochim. Ac. 104, 281-299.
692 Louvel, M., Sanchez-Valle, C., Malfait, W.J., Testemale, D. and Hazemann, J-L., 2014. Constraints on
693 the mobilization of Zr in magmatic-hydrothermal processes in subduction zones from in situ fluid-
694 melt partitioning experiments. Am. Mineral. 99, 1616-1625.
695 Louvel, M., Cadoux, A., Brooker, R., Proux, Olivier and Hazemann, J-L., 2020 New insights on Br
696 speciation in volcanic glasses and structural controls on halogens degassing. *In press,.Am. Mineral.*
697 10.2138/am-2020-7273
698 Makino, Y., 1995. Correlation between Pseudopotential Radii and Interatomic Distance and Evaluation of
699 Bond Characters for Transition and Lanthanide Elements. J. Alloy. Compd. 227, 18-27.
700 Manning, C. E., 2004. The chemistry of subduction-zone fluids. Earth Planet. Sc. Lett. 223, 1-16.
701 Mayanovic, R. A., Anderson, A. J., Bassett, W. A., and Chou, I. M., 2001. Hydrogen bond breaking in
702 aqueous solutions near the critical point. Chem. Phys. Lett. 336, 212-218.
703 McKeown, D. A., Gan, H., Pegg, I. L., Stolte, W. C., and Demchenko, I. N., 2011. X-ray absorption
704 studies of chlorine valence and local environments in borosilicate waste glasses. J. Nucl. Mater.
705 408, 236-245.

McKeown, D.A., Muller, I.S. and Pegg, I.L., 2015. Iodine valence and local environments in borosilicate waste glasses using X-ray absorption spectroscopy. J. Nucl. Mater. 456, 182-191.

Mustre de Leon, J., Rehr, J. J., Zabinsky, S. I., and Albers, R. C., 1991. Ab initio curved-wave X-ray-absorption fine structure. Phys. Rev. B 44, 4146-56.

Mysen, B. O. and Cody, G. D., 2004. Solubility and solution mechanism of H_2O in alkali silicate melts and glasses at high pressure and temperature. Geochim. Cosmochim. Ac. 68, 5113-5126.

Mysen, B.O. and Wheeler, K., 2000. Solubility behavior of water in haploandesitic melts at high pressure and high temperature. Am. Mineral. 85, 1128-1142.

Newville, M., 2001. EXAFS analysis using FEFF and FEFFIT. J. Synchrotron Radiat. 8, 96-100.

Pan, D., Spanu, L., Harrison, B., Sverjensky, D.A. and Galli, G., 2013. Dielectric properties of water under extreme conditions and transport of carbonates in the deep Earth. PNAS 110, 6646-6650.

Pokrovski G.S., Borisova A.Y., Harrichoury J.-C. (2008) The effect of sulfur on vapor-liquid fractionation of metals in hydrothermal systems. Earth Planet. Sc. Lett. 266 (3-4), 345-362.

Pokrovski, G. S., Tagirov, B. R., Schott, J., Hazemann, J. L., and Proux, O., 2009a. A new view on gold speciation in sulfur-bearing hydrothermal fluids from in situ X-ray absorption spectroscopy and quantum-chemical modeling. Geochim. Cosmochim. Ac. 73, 5406-5427.

Pokrovski, G. S., Tagirov, B. R., Schott, J., Bazarkina, E. F., Hazermann, J. L., and Proux, O., 2009b. An in situ X-ray absorption spectroscopy study of gold-chloride complexing in hydrothermal fluids. Chem. Geol. 259, 17-29.

Pokrovski G.S., Borisova A.Y., Bychkov A.Y. (2013) Speciation and transport of metals and metalloids in geological vapors. Book chapter 6 in: Thermodynamics of Geothermal Fluids (eds. A. Stefánsson, T. Driesner, P. Bénézeth). Rev. Miner. Geochem. 76, 165-218.

Pyle, D. M. and Mather, T. A., 2009. Halogens in igneous processes and their fluxes to the atmosphere and oceans from volcanic activity: A review. Chem. Geol. 263, 110-121.

Ramos, S., Barnes, A. C., Neilson, G. W., Thiaudiere, D., and Lequien, S., 2000. The hydration structure of Br- from anomalous x-ray diffraction. J. Phys.-Condens. Mat. 12, A203-A208.

732 Ravel, B. and Newville, M., 2005. ATHENA, ARTEMIS, HEPHAESTUS: data analysis for X-ray
733 absorption spectroscopy using IFEFFIT. J. Synchrotron Radiat. 12, 537-541.
734 Roberge, M., Bureau, H., Bolfan-Cassanova, N., Frost, D.J., Raepsaet, C., Surble,S., Khodja, H.,
735 Auzende, A-L. and Fiquet, G., 2015. Is the transition zone a deep reservoir for fluorine? Earth
736 Planet. Sc. Lett. 429, 25-32.
737 Rustioni, G., Audetat, A. and Keppler, H., 2019. Experimental evidence for fluid-induced melting in
738 subudction zones. Geochem. Perspect. Lett.
739 Sanchez-Valle, C., 2013. Structure and thermodynamics of subduction zone fluids from spectroscopic
740 studies. Rev. Mineral. Geochem. 76, 265-309.
741 Sanchez-Valle, C., Martinez, I., Daniel, I., Philippot, P., Bohic, S., and Simionovici, A., 2003. Dissolution
742 of strontianite at high P-T conditions: An in-situ synchrotron X-ray fluorescence study. Am.
743 Mineral. 88, 978-985.
744 Sanchez-Valle, C., Daniel, I., Martinez, I., Simionovici, A., and Reynard, B., 2004. Progress in
745 quantitative elemental analyses in high P-T fluids using synchrotron x-ray fluorescence (SXRF). J.
746 Phys.-Condens. Mat. 16, S1197-S1206.
747 Sandland, T. O., Du, L. S., Stebbins, F., and Webster, J. D., 2004. Structure of Cl-containing silicate and
748 aluminosilicate glasses: A ^{35}Cl MAS-NMR study. Geochim. Cosmochim. Ac. 68, 5059-5069.
749 Sherman, D.M., 2010. Metal complexation and ion association in hydrothermal fluids: insights from
750 quantum chemistry and molecular dynamics. Geofluids 10, 41-57.
751 Signorelli, S. and Carroll, M. R., 2002. Experimental study of Cl solubility in hydrous alkaline melts:
752 constraints on the theoretical maximum amount of Cl in trachytic and phonolitic melts. Contrib.
753 Mineral. Petr. 143, 209-218.
754 Silvestrelli, P. L. and Parrinello, M., 1999. Structural, electronic, and bonding properties of liquid water
755 from first principles. J. Chem. Phys. 111, 3572-3580.
756 Skora, S. and Blundy, J., 2010. High-pressure hydrous phase relations of radiolarian clay and implications
757 for the involvement of subducted sediment in arc magmatism. J. Pet. 51, 2211-2243.

758 Soper, A. K. and Benmore, C. J., 2008. Quantum Differences between Heavy and Light Water. Phys.
759 Rev. Lett. 101, 065502-1-4.
760 Stebbins, J. F. and Du, L. S., 2002. Chloride ion sites in silicate and aluminosilicate glasses: A
761 preliminary study by Cl-35 solid-state NMR. Am. Mineral. 87, 359-363.
762 Stolper, E., 1982. Water in silicate glasses: An infrared spectroscopic study. Contrib. Mineral. Petr. 81,
763 1-17.
764 Sverjensky, D.A., Harrison, B. and Azzolini, D., 2014. Water in the deep Earth : The dielectric constant
765 and the solubilities of quartz and corundum to 60 kb and 1200 C. Geochim. Cosmochim. Ac. 129,
766 125-145.
767 Uchino, T., Sakka, T., Ogata, Y., and Iwasaki, M., 1992. Mechanism of hydration of sodium-silicate glass
768 in a steam environment - Si^{29} NMR and ab initio molecular-orbital studies. Journal of Physical
769 Chemistry 96, 7308-7315.
770 van Sijl, J., Allan, N. L., Davies, G. R., and van Westrenen, W., 2010. Titanium in subduction zone
771 fluids: First insights from ab initio molecular metadynamics simulations. Geochim. Cosmochim.
772 Ac. 74, 2797-2810.
773 Von Glasow, R., Bobrovski, N. and Kern, C., 2009. The effects of volcanic eruptions on atmospheric
774 chemistry. Chem. Geol. 263, 131-142.
775 Wallace, P. J., 2005. Volatiles in subduction zone magmas: concentrations and fluxes based on melt
776 inclusion and volcanic gas data. J. Volcanol. Geoth. Res. 140, 217-240.
777 Wallen, S. L., Palmer, B. J., Pfund, D. M., Fulton, J. L., Newville, M., Ma, Y. J., and Stern, E. A., 1997.
778 Hydration of bromide ion in supercritical water: An X-ray absorption fine structure and molecular
779 dynamics study. J. Phys. Chem. A 101, 9632-9640.
780 Wasik, A., Dingwell, D.B., Courtial, P. and Hess, K., 2005. Viscosity and chemical diffusion of halogens
781 in silicate melts: implications for volcanic degassing. Eos Trans. AGU 86 (52) Fall Meet. Suppl.,
782 Abstract V21E-0667.

783 Webster, J. D., 1990. Partitioning of F between H_2O and CO_2 fluids and topaz rhyolite melt - Implications
784 for mineralizing magmatic-hydrothermal fluids in F-rich granitic systems. Contrib. Mineral. Petr.
785 104, 424-438.
786 Webster, J. D., 1992. Water Solubility and Chlorine Partitioning in Cl-Rich Granitic Systems - Effects of
787 Melt Composition at 2 kbar and 800 °C. Geochim. Cosmochim. Ac. 56, 679-687.
788 Webster, J. D. and Holloway, J. R., 1988. Experimental constrains on the partitioning of Cl between
789 Topaz Rhyolite melt and H_2O and H_2O+CO_2 fluids. New Implications for granitic differentiation
790 and ore deposition. Geochim. Cosmochim. Ac. 52, 2091-2105.
791 Webster, J. D. and De Vivo, B., 2002. Experimental and modeled solubilities of chlorine in
792 aluminosilicate melts, consequences of magma evolution, and implications for exsolution of
793 hydrous chloride melt at Mt. Somma-Vesuvius. Am. Mineral. 87, 1046-1061.
794 Webster, J.D., Kinzler, R.J. and Mathez, E.A., 1999. Chloride and water solubility in basalt and andesite
795 melts and implications for magmatic degassing. Geochim. Cosmochim. Ac. 63, 729-738.
796 Webster, J. D., Sintoni, M. F., and De Vivo, B., 2009. The partitioning behavior of Cl, S, and H_2O in
797 aqueous vapor-± saline-liquid saturated phonolitic and trachytic melts at 200 MPa. Chem. Geol.
798 263, 19-36.
799 **Wohlers, A., Manning, C.E. and Thompson, A.B. 2011. Experimental investigation of the solubility**
800 **of albite and jadeite in H2O, with paragonite + quartz at 500 and 600 °C, and 1-2.25 GPa.**
801 **Geochim. Cosmochim. Ac. 75, 2924-2939.**
802 Xue, X. Y. and Kanzaki, M., 2004. Dissolution mechanisms of water in depolymerized silicate melts:
803 Constraints from H-1 and Si-29 NMR spectroscopy and ab initio calculations. Geochim.
804 Cosmochim. Ac. 68, 5027-5057.
805 Yamashita, S., Behrens, H., Schmidt, B. C., and Dupree, R., 2008. Water speciation in sodium silicate
806 glasses based on NIR and NMR spectroscopy. Chem. Geol. 256, 231-241.
807
808

809 # List of Tables and Figure captions:

810

811 **Table1.** Synthesis conditions and chemical compositions of the $Na_2Si_2O_5$ (NS2) and haplogranite (Hpg)
812 glasses employed as starting materials in this study.

813

814 **Table 2:** Bromine fluid-melt partition coefficients at different P-T conditions. Calculated fluid and melt
815 compositions and densities are also reported.

816

817 **Table 3.** Structural parameters derived from Br K-edge EXAFS analysis for the reference aqueous
818 solutions and silicate glasses at ambient conditions.

819

820 **Table 4:** Br K-edge EXAFS analysis of experimental high P-T fluids with various compositions.

821

822

823 **Figure 1.** Microphotographs of the compression chamber of the HDAC showing the Haplogranite - H_2O
824 (A, B, C) and NS2 - H_2O (D, E, F) systems at the indicated pressure and temperature conditions. Images
825 are taken through the diamond along the X-ray path. A) Haplogranite glass and 3 wt% NaBr aqueous
826 solution at room conditions; B) globulus of hydrous silicate melt in equilibrium with the aqueous fluid; C)
827 supercritical liquid (single fluid phase); D) NS2 glass and 3 wt% NaBr aqueous solution at room
828 conditions; E) supercritical liquid (low temperature supercriticality); F) hydrous NS2 melt coexisting with
829 aqueous fluid (high temperature subcriticallity).

830

831 **Figure 2.** 2D-SXRF Br K_α intensity maps of Run 1 showing the distribution of Br between coexisting
832 aqueous fluid and haplogranite melt at different P-T conditions. The fluid:glass ratio refers to the wt

fraction calculated from the volumetric proportions of loaded glass and sample chamber. The white dashed line delimits the edge of the Re gasket.

Br-enriched phases appear in red and yellow, Br-depleted areas in blue and green. At the beginning of the experiment (A), all the Br is concentrated in the glass. After the glass melts (B), Br strongly partitions into the fluid phase ($D_{Br}^{f/m}$ = 8.07 ±0.79). As temperature increases, the Br concentration in the melt increases while the Br concentrations in the fluid decreases (C). At 821°C - 0.9GPa, the I_f/I_m ratio appears homogeneous as the Br concentrations per volume are almost similar (I_f/I_m = 1.3 ±0.1). However, per weight, Br still partitions preferentially into the fluid ($D_{Br}^{f/m}$ = 2.02 ±0.14).

Figure 3. Evolution of the Br partition coefficients $D_{Br}^{f/m}$ with increasing temperature at different pressure conditions. The different symbols and colors account for separate experimental runs involving different glass proportions. The errors reported on $D_{Br}^{f/m}$ take into account the uncertainties on pressure determination (10%) and on the determination of fluid and melt composition and density from previous studies. The partition coefficients from Bureau et al. (2010) and Cadoux et al. (2018) are shown for comparison. For Cadoux et al., note that both average values from several experiments ($D_{Br}^{f/m}$ = 20.2 ±1.2) and minimum value for a single experiment ($D_{Br}^{f/m}$ = 8.6) are reported.

Figure 4. Normalized Br K-edge XANES spectra collected on Br-bearing silicate glasses, aqueous fluids and hydrous silicate melts at various pressure and temperature conditions. Spectra are offset for clarity. The vertical dashed line is a visual guide to appreciate phase shifts. The black arrow shows the pre-edge feature in the haplogranite glass spectrum corresponding to the 1s to 4p transition in Br (Burattini et al., 1991).

Figure 5. Normalized k^1-weighted EXAFS oscillations of the investigated Br-bearing samples (black solid lines) and corresponding least-square fits (blue dashed lines). Spectra are off-set vertically for clarity. The pressure and temperature conditions and the compositions are reported right to each spectrum. **The dashed lines underline the shift of EXAFS oscillations with change in composition.**

Figure 6. Evolution of bromine coordination numbers with oxygen (from H_2O molecules) and sodium ($N_{Br\cdots H\text{-}O}$ and $N_{Br\text{-}Na}$) as a function of fluid composition (*i.e*, the weight fraction of NS2 dissolved in the fluid) along the NaBr aqueous solution – NS2 join. The gray field shows the detection limit (DL) for Br-Na complexes, which corresponds to the maximum Br-Na coordination number ($N_{Br\text{-}Na}$) determined for 3wt% NaBr aqueous solution at ambient conditions and 450 °C (DL < 1.5 atoms).

Table 1.

Sample	Synthesis conditions T (°C)	P(GPa)	Br[1] (wt%)	Na_2O[2] (wt%)	SiO_2[2] (wt%)	Al_2O_3[2] (wt%)	K_2O[2] (wt%)	H_2O[3] (wt%)	ASI[4]	Analytical method
NS2-Br1	1200	0.5	4.01 4.10	32.0	63.9					EMPA LA-ICPMS
Hpg-Br2	1200	1.5	- 0.96	7.1	74.1	9.2	3.7	3.3	0.57	EMPA RBS
Hpg-Br3	1200	1.5	0.89	7.4	75.0	9.4	3.8	3.3	0.57	EMPA

Notes: EMPA = Electron Microprobe Analyses; **LA-ICPMS =** Laser-ablation Inductively Couple Plasma Mass Spectrometry; **RBS** = Rutherford Backscattering Spectroscopy.

[1]Standard deviations (1σ) are 0.04 wt% for RBS analysis, 0.3 wt% for LA-ICPMS and 0.03 wt% for EMPA analysis.

[2]Average from 10 to 25 analyses performed on each glass composition. Standard deviations (1σ) are < 0.1 wt% for Na_2O, Al_2O_3 and K_2O and < 0.3 wt% for SiO_2.

[3]Nominal H_2O concentration (not analyzed).

[4]Aluminum Saturation Index ASI = $\frac{Al_2O_3}{Na_2O+K_2O}$ (in moles).

Table 2.

X_g [1]	T (°C)	P (GPa) [2]	H_2O in melt (wt%) [3]	Melt density ρ_m [4]	Transmission in melt T_m	Silicates in fluid (wt%) [5]	Fluid density ρ_f [7]	Transmission in fluid T_f	I_{Br}^{f} / I_{Br}^{m}	$D_{Br}^{f/m}$
Haplogranite – H_2O										
Run 1										
0.76	592	0.7	7.1 ±0.8	2.24	0.66	2.5 ±0.5	0.94	0.96	4.9	**8.1** ±0.8
	694	0.8	7.7 ±0.9	2.23	0.67	5.3 ±1.2	0.97	0.95	2.6	**4.2** ±0.2
	821	0.9	8.0 ±1.0	2.23	0.67	10.3 ±2.3	0.99	0.95	1.3	**2.0** ±0.1
Run 2										
0.82	645	0.9	9.1 ±1.1	2.22	0.67	5.5 ±1.1	1.02	0.95	10.0	**15.3** ±1.0
	710	1.1	11.1 ±1.4	2.20	0.68	11.1 ±2.4	1.09	0.94	5.4	**7.9** ±0.5
	840	0.9	7.9 ±1.0	2.23	0.67	10.8 ±2.4	0.98	0.95	2.8	**4.4** ±0.3
Run 3										
0.72	610	1.2	13.3 ±1.7	2.18	0.69	7.7 ±1.6	1.13	0.95	4.6	**6.4** ±0.3
	730	0.65	6.0 ±0.7	2.25	0.66	3.9 ±0.9	0.88	0.96	2.3	**4.1** ±0.4
	800	0.2	2.4 ±0.2	2.26	0.64	0.7 <0.1	0.49	0.98	1.6	**4.8** ±0.3
Haplogranite – 3 wt% NaBr aqueous solution										
Run 4										
0.70	740	1.7	19.5 ±2.8	2.11 ±0.02	0.72	12.8 ±0.8 [6]	1.20	0.94	7.2	**9.7** ±0.6
Error (unless indicated)		±0.1		±0.01	±0.07		±0.04	±0.01	±0.04-0.43	

Notes:

[1] Initial weight fraction of glass in the loading.

[2] Maximum uncertainty on pressure were of 10%.

[3] H_2O solubility in the haplogranite melt calculated from the solubility data of Mysen and Wheeler (2000).

[4] Melt density (in $g.cm^{-3}$) calculated as a function of P-T conditions and melt composition using Malfait et al. (2014).

[5] Solubility of silicate components (SiO_2, Na_2O, Al_2O_3 and K_2O)in the aqueous fluid coexisting with haplogranite melt calculated from the albite solubility data of Anderson and Burnham (1983).

[6] Silicate solubility in the aqueous fluid estimated from Wohlers et al. (2011) for P > 1.2 GPa.

[7] Fluid density (in $g.cm^{-3}$) calculated as a function of P-T conditions from the data of Mantegazzi et al. (2013)

910

911 **Table 3.**

Composition	Oxygen (O)			Sodium (Na)			
Aqueous solutions[1]							
	$N_{Br\cdots H\text{-}O}$	$R_{Br\cdots H\text{-}O}$ (Å)	σ^2 (Å^2)				*R-factor*
3 wt% NaBr-H_2O	5.9 ±0.7	3.37 ±0.04	0.02				0.04
2.3 wt% KBr-H_2O.[3]	5.7 ±0.8	3.30 ±0.03	0.02				0.06
Silicate glasses[2]							
	$N_{Br\text{-}O}$	$R_{Br\text{-}O}$ (Å)	σ^2 (Å^2)	$N_{Br\text{-}Na}$	$R_{Br\text{-}Na}$ (Å)	σ^2 (Å^2)	*R-factor*
NS2 glass	5.2 ±2.4	3.45 ±0.09	0.02	5.3 ±1.8	2.99 ±0.09	0.03	0.25
Haplogranite glass	6.1 ±3.6	3.39 ±0.03	0.02	5.9 ±1.8	2.94 ±0.03	0.03	0.21

912

913 **Notes:** N = Br coordination number ($N_{Br\text{-}O}$ or $N_{Br\text{-}Na}$); R = Br-neighbor (Na or O) mean distance (Å); σ^2 = squared Debye-Waller
914 factor (Å^2); *R-factor* = goodness of the fit; $S_0^2 = 1$;
915 [1] Hydration shell (Br···H-O)
916 [2] Br coordinated to oxygens from the silicate network (next-nearest coordination shell).
917 [3] Ferlat et al. (2002), 0.2m KBr-H_2O for comparison.
918

Table 4.

Composition	T (°C)	P (GPa)	$N_{Br\cdots H\text{-}O}$	$R_{Br\cdots H\text{-}O}$ (Å)	σ^2 (Å^2)	$N_{Br\text{-}Na}$	$R_{Br\text{-}Na}$ (Å)	σ^2 (Å^2)	*R-factor*
3 wt% NaBr aqueous solution									
	25	0	5.9 ± 0.7	3.37 ±0.04	0.02	bdl[1]			0.04
	320	0.2	6.3 ± 1.8	3.36 ±0.05	0.04	bdl			0.17
	450	0.6	6.4 ±1.1	3.40 ±0.07	0.05	bdl			0.19
Br-bearing aqueous fluids									
1.2 wt% Hpg[3]	475	1	5.4 ±0.9	3.33 ±0.03	0.05	bdl			0.13
5 wt% Hpg	680	0.8	5.7 ±1.1	3.30 ±0.04	0.06	bdl			0.12
0.6 wt% Hpg	750	0.2	5.0 ±1.6	3.33 ±0.06	0.06	bdl			0.30
30 wt% NS2[2]	190	n.d.	6.7 ±1.4	3.38 ±0.03	0.04	bdl			0.14
	320	n.d.	5.7 ±1.4	3.37 ±0.09	0.04	bdl			0.22
50 wt% NS2	580	1.1	4.7 ±1.5	3.35 ±0.15	0.04	bdl			0.25
Br-bearing melt-like fluids									
60 wt% NS2	480	1.5	3.6 ±1.5	3.47 ±0.05	0.01	2.5 ±1.2	3.10 ±0.06	0.01	0.23
	610	2.2	4.8 ±2.4	3.45 ±0.05	0.03	2.6 ±0.9	3.06 ±0.06	0.03	0.20
NS2 melt (10 ±1 wt% H_2O)	710	0.4	3.4 ±1.6	3.36 ±0.03	0.02	6.6 ±2.1	2.91 ±0.03	0.05	0.24

Notes: N = Br coordination number (dissociate as $N_{Br\cdots H\text{-}O}$ and $N_{Br\text{-}Na}$); R = Br-neighbor mean distance (Å); σ^2 = squared Debye-Waller factor (Å^2); *R-factor* = goodness of the fit; $S_0^2 = 1$.

[1]bdl = below detection limit. Detection limit corresponds to the maximum Br-Na coordination number determined for 3 wt% NaBr aqueous solution at ambient conditions.

[2]wt% NS2 indicates the amount of dissolved NS2 in the single phase fluid calculated from the mass of H_2O and NS2 glass.

[3]wt% Hpg refers to the amount of dissolved silicate in the fluid coexisting with haplogranite melt calculated as in Table 2.

Errors in temperature and pressure are ±2 ºC and 10%, respectively. Errors in the composition of the analyzed fluids are within 5% (Table 2).

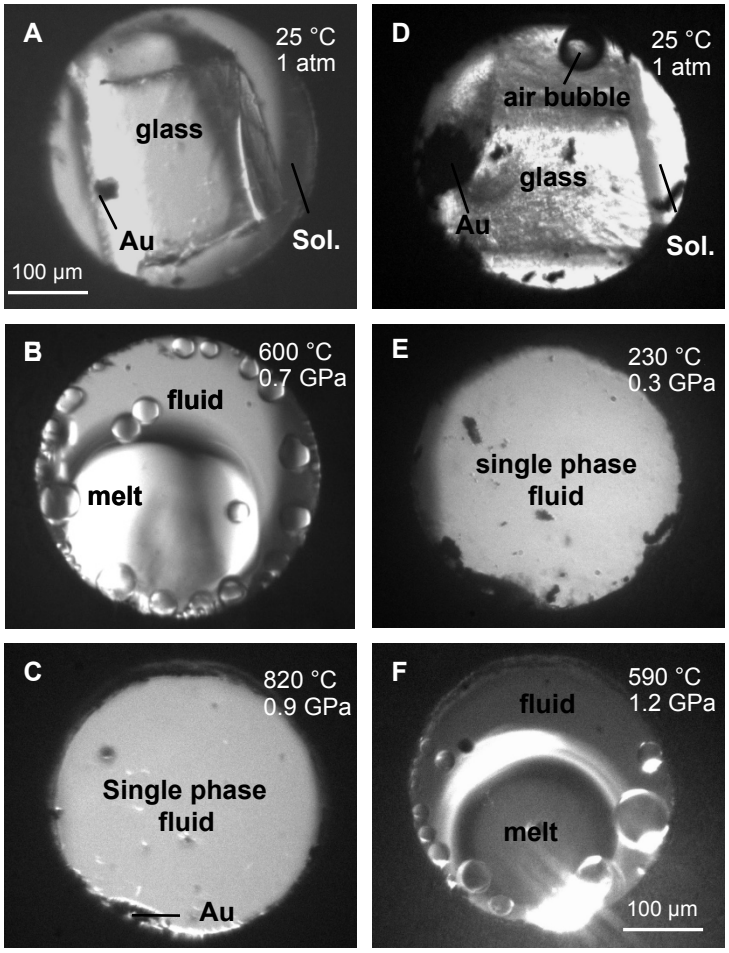
A
25 °C
1 atm
glass
Au
Sol.
100 µm
D
25 °C
1 atm
air bubble
glass
Au
Sol.
B
600 °C
0.7 GPa
fluid
melt
E
230 °C
0.3 GPa
single phase
fluid
C
820 °C
0.9 GPa
Single phase
fluid
Au
F
590 °C
1.2 GPa
fluid
melt
100 µm

Figure 1

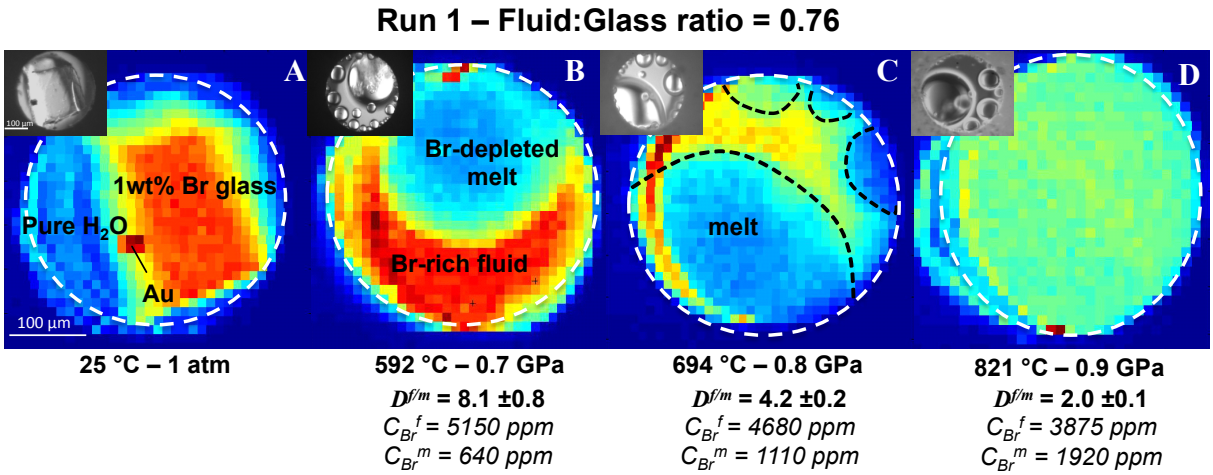
Run 1 – Fluid:Glass ratio = 0.76
A
B
C
D
1wt% Br glass
Pure H2O
Au
100 µm
Br-depleted melt
Br-rich fluid
melt
25 °C – 1 atm
592 °C – 0.7 GPa
D^f/m = 8.1 ±0.8
C_Br^f = 5150 ppm
C_Br^m = 640 ppm
694 °C – 0.8 GPa
D^f/m = 4.2 ±0.2
C_Br^f = 4680 ppm
C_Br^m = 1110 ppm
821 °C – 0.9 GPa
D^f/m = 2.0 ±0.1
C_Br^f = 3875 ppm
C_Br^m = 1920 ppm

Figure 2

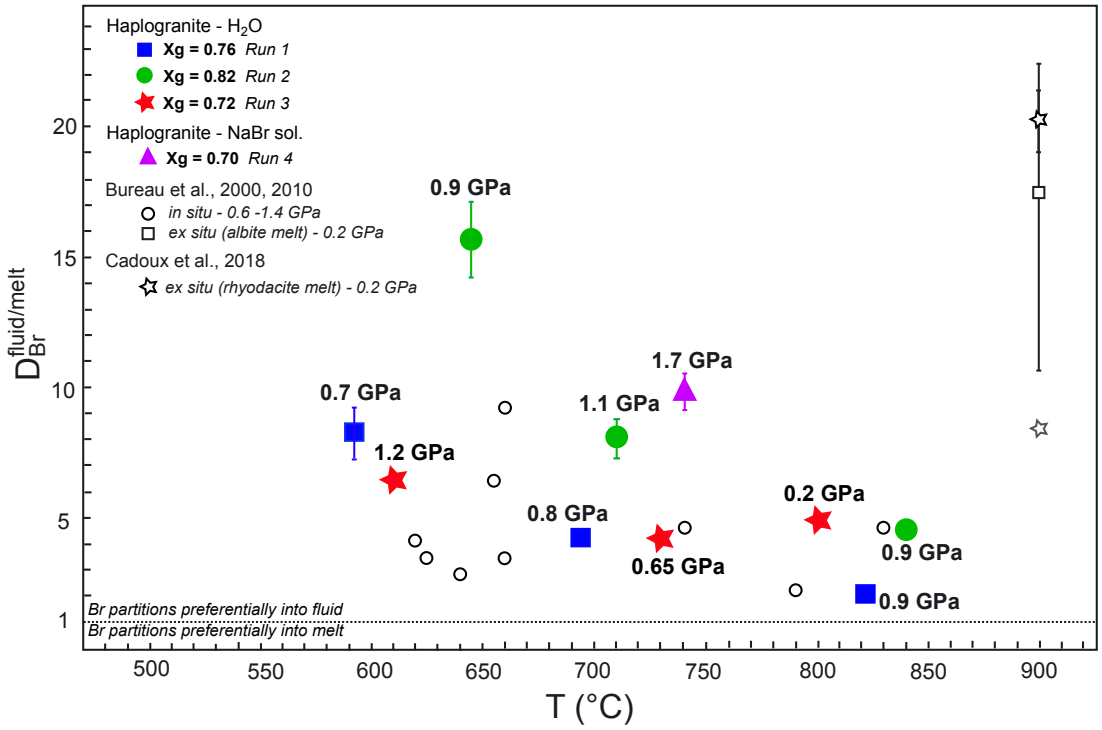
Haplogranite - H2O
Xg = 0.76 Run 1
Xg = 0.82 Run 2
Xg = 0.72 Run 3
Haplogranite - NaBr sol.
Xg = 0.70 Run 4
Bureau et al., 2000, 2010
in situ - 0.6 -1.4 GPa
ex situ (albite melt) - 0.2 GPa
Cadoux et al., 2018
ex situ (rhyodacite melt) - 0.2 GPa
0.9 GPa
1.7 GPa
0.7 GPa
1.1 GPa
1.2 GPa
0.2 GPa
0.8 GPa
0.9 GPa
0.65 GPa
0.9 GPa
Br partitions preferentially into fluid
Br partitions preferentially into melt
D fluid/melt Br
T (°C)
1
5
10
15
20
500
550
600
650
700
750
800
850
900

Figure 3

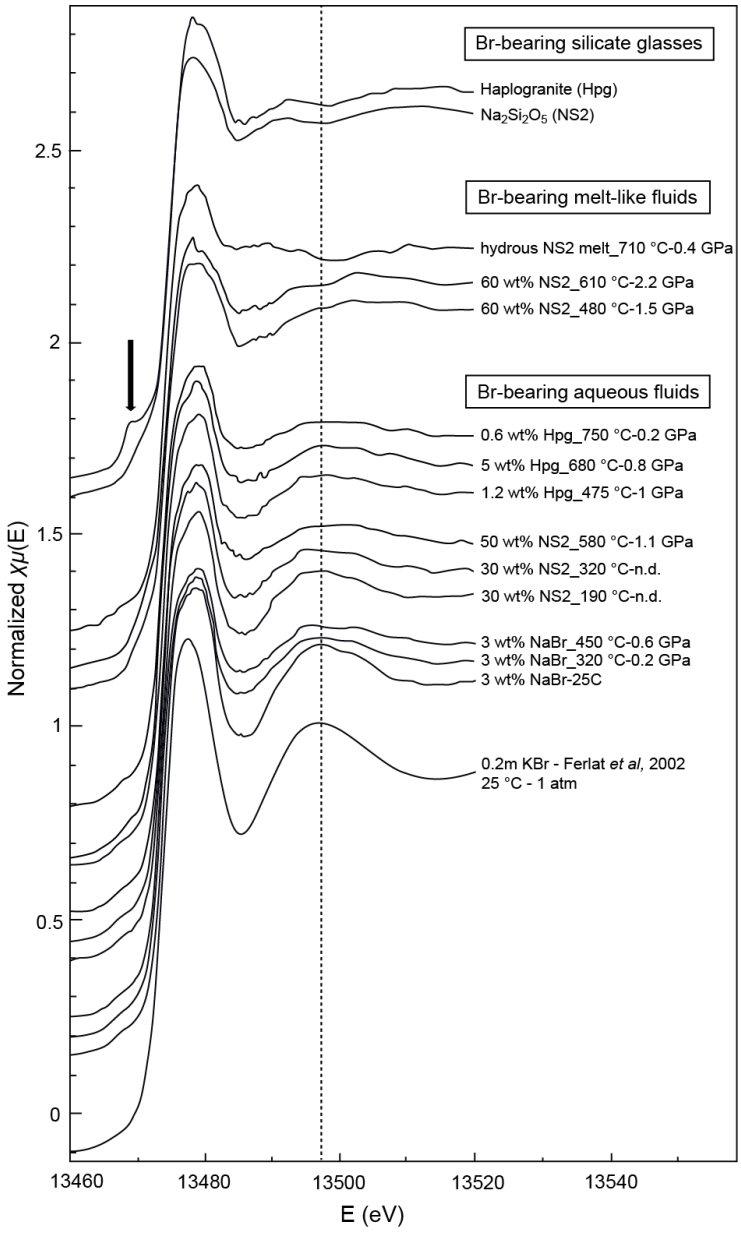
Br-bearing silicate glasses
Haplogranite (Hpg)
$Na_2Si_2O_5$ (NS2)
Br-bearing melt-like fluids
hydrous NS2 melt_710 °C-0.4 GPa
60 wt% NS2_610 °C-2.2 GPa
60 wt% NS2_480 °C-1.5 GPa
Br-bearing aqueous fluids
0.6 wt% Hpg_750 °C-0.2 GPa
5 wt% Hpg_680 °C-0.8 GPa
1.2 wt% Hpg_475 °C-1 GPa
50 wt% NS2_580 °C-1.1 GPa
30 wt% NS2_320 °C-n.d.
30 wt% NS2_190 °C-n.d.
3 wt% NaBr_450 °C-0.6 GPa
3 wt% NaBr_320 °C-0.2 GPa
3 wt% NaBr-25C
0.2m KBr - Ferlat *et al*, 2002
25 °C - 1 atm
Normalized χμ(E)
E (eV)
0
0.5
1
1.5
2
2.5
13460
13480
13500
13520
13540

Figure 4

998

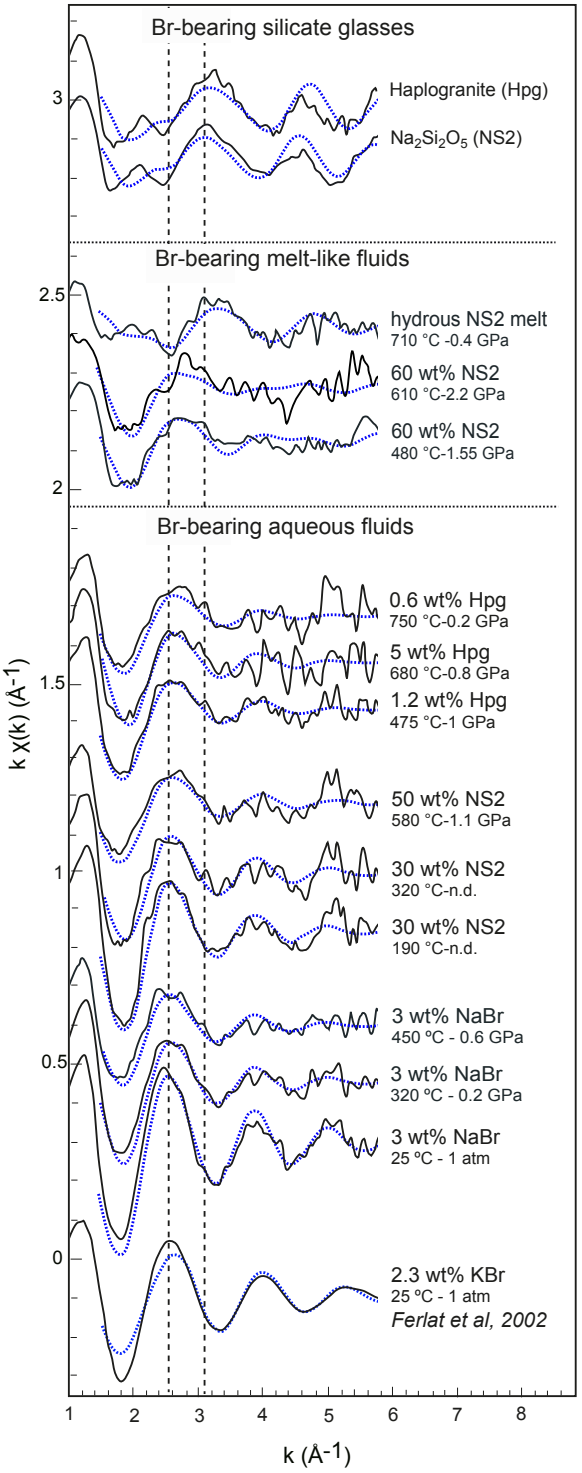

999

1000 **Figure 5**

1001

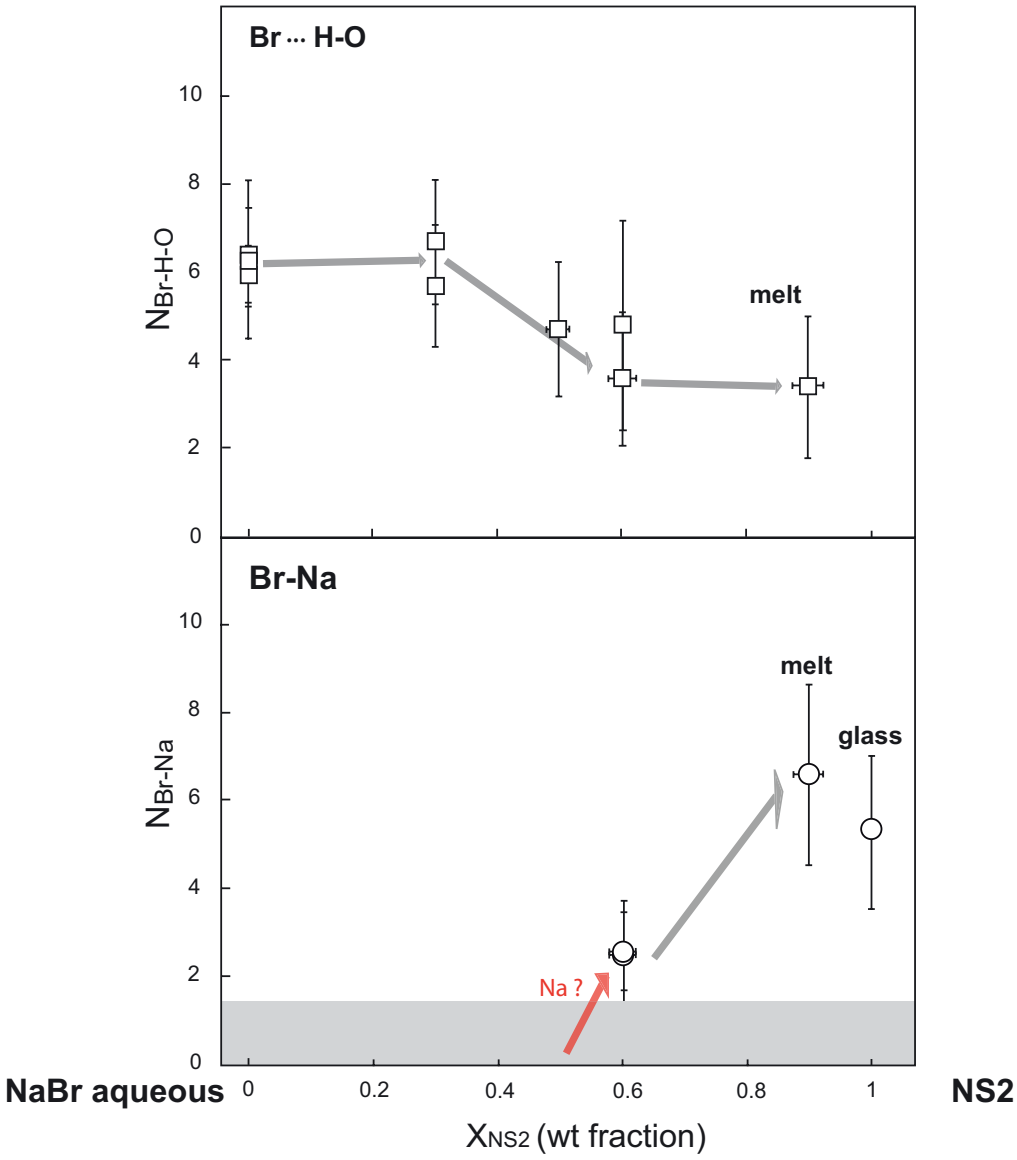

1002

1003

1004 **Figure 6**